VLA IMAGING OF FANAROFF–RILEY II 3CR RADIO GALAXIES. II. EIGHT NEW IMAGES AND COMPARISONS WITH 3CR QUASARS

ILIAS FERNINI[1] AND JACK O. BURNS[2]
Department of Astronomy, New Mexico State University, Las Cruces, New Mexico 88003
Electronic mail: ifernini@nyx.uaeu.ac.ae, burns@research.missouri.edu

RICK A. PERLEY
National Radio Astronomy Observatory,[3] P.O. Box O, Socorro, New Mexico 87801
Electronic mail: rperley@nrao.edu

Received 1997 July 25; revised 1997 August 25; accepted 1997 August 26

ABSTRACT

We report the results of VLA observations of eight classical double radio galaxies (RGs). Paper I (Fernini *et al.* 1993, AJ, 105, 1690) presented images and preliminary analysis for five other RGs. We now have a statistically complete sample of RGs with which we can compare to a similarly imaged sample of quasars (QSRs) from Bridle *et al.* (1994, AJ, 108, 766). A radio jet is seen only in one RG, 3C 441. Combined with the results of Paper I, the jet detection rate stands at only two, one of which was recently shown to have a broad Hα line, and no counterjet detection. Our low jet detection rate for RGs contrasts strongly with the 100% jet detection and the 50% candidate counterjet detection in the QSRs. We have detected compact central features in ten RGs, eight for the first time. We found that the QSRs have much stronger compact central features than the RGs, a result consistent with previous observations. The median of the ratio of the compact central feature to extended flux densities is 0.7% and 4% for the RGs and the QSRs, respectively. The QSR hot spots are slightly more compact than the RG hot spots. We discuss the implications of these results in the light of the RG/QSR unification scheme of Barthel (1989, ApJ, 336, 606). © *1997 American Astronomical Society.* [S0004-6256(97)01612-9]

1. INTRODUCTION

In Fernini *et al.* (1993, Paper I), we presented the results of our first VLA observations allocated to the study of jets and counterjets in powerful extended radio galaxies (FR Type II sources—Fanaroff & Riley 1974). Five classical double radio galaxies (RGs) out of a sample of thirteen were reported in that paper. This paper presents results for the remaining eight sources observed at 5 GHz.

The observations of these 13 FR II radio galaxies and of the 13 FR II quasars of Bridle *et al.* (1994) were made to test the unification model of Barthel (1989). This model proposes that radio-loud quasars and classical double radio galaxies belong to the same parent population of objects. The key physical process behind the unification is relativistic beaming (e.g., Rees 1978; Scheuer & Readhead 1979; Blandford & Königl 1979). Within the context of this scheme, the differences in morphologies and prominence of structures (jet, compact central feature, and hot spots) between these two types of objects are related to their orientation with respect to the line of sight. The transition from radio galaxy to quasar properties is suggested to occur around 44° to the line of sight.

According to this model, in FR II quasars the synchrotron emission of the approaching jet is beamed towards, and that of the receding counterjet beamed away from the observer. In FR II radio galaxies, whose radio axes lie closer to the plane of the sky, the synchrotron emission of both jets is less beamed, or even suppressed, and thus more difficult to detect. The quasar jets are therefore predicted to be more prominent relative to their lobes than those in the RGs, and Barthel's unification predicts that the jet/counterjet ratios in RGs should be smaller than in the quasars, both on the large scale and the small scale.

Two studies have been undertaken to test the above RG/QSR unification scheme: one by Bridle *et al.* (1994) for the QSRs, and the other by Fernini *et al.* (1993 and this paper) for the RGs. Two statistically-comparable samples of 13 sources each have been observed with the VLA *A* and *B* configurations using long integration times in order to obtain images with high dynamic range and good angular resolution. These two requirements are necessary to detect low surface brightness emission yet still distinguish jets from other features.

Paper I reported the high resolution 5 GHz observations of five FR II RGs: 3C 22, 3C 55, 3C 265, 3C 324, and 3C 356. We detected the compact central radio features of at least four RGs—three for the first time—but a definite radio

[1]Current address: Department of Physics, United Arab Emirates University, P.O. Box #17551, Al-Ain, U.A.E.
[2]Current address: Office of Research, 205 Jesse Hall, University of Missouri, Columbia, MO 65221.
[3]The National Radio Astronomy Observatory is a facility of the National Science Foundation, operated under a cooperative agreement by Associated Universities, Inc.

TABLE 1. Basic properties of the radio-galaxy sample.

IAU NAME	3C NAME	z	LAS ($''$)	l (kpc)	S_{5GHz} (Jy)	$\log(L_{5GHz})$ (W/Hz)
0040+517	3C 20*	0.174	51	204	4.18	26.14
0048+509	3C 22**	0.937	24	135	0.76	26.9
0107+315	3C 34	0.689	48	254	0.43	26.5
0125+287	3C 42	0.395	28	119	0.84	26.2
0154+286	3C 55	0.7348	69	372	0.88	26.8
1030+585	3C 244.1	0.428	51	226	1.12	26.4
1108+359	3C 252	1.1035	57	326	0.32	26.8
1142+318	3C 265	0.811	78	429	0.63	26.8
1547+215	3C 324	1.2063	10	57	0.61	27.1
1549+628	3C 325	0.86	16	89	0.83	26.9
1609+660	3C 330	0.550	56	276	2.35	26.9
1723+510	3C 356	1.079	75	429	0.38	26.8
2203+292	3C 441	0.707	29	155	0.92	26.8

Notes to Table 1

* Redshift of 3C 20, reported in paper I, has been changed to 0.174 (Sec.3.1)

** 3C 22 shows a quasar-like nucleus (Economou *et al.* 1995).

TABLE 2. Observing log of the second sample of RGs (S2).

Source	Date	Config.	Bandw. (MHz)	Int.Time (min.)
3C 20	07/17/91	A	25	170
	12/22/91	B	25	80
3C 34	07/17/91	A	25	170
	12/22/91	B	25	80
3C 42	07/20/91	A	50	168
	12/22/91	B	50	80
3C 244.1	08/04/91	A	25	156
	12/23/91	B	25	88
3C 252	08/04/91	A	25	156
	12/23/91	B	25	84
3C 325	07/20/91	A	50	144
	12/23/91	B	50	88
3C 330	07/20/91	A	25	144
	12/23/91	B	25	88
3C 441	07/20/91	A	50	168
	12/22/91	B	50	80

jet was detected only in 3C 22, and no counterjet candidates were found. Candidate jets (or jet components) were found in 3C 55, 3C 265, and 3C 324, but in all three there is a strong possibility of confusion with lobe edge-brightening or filaments.

These results for the RGs contrast with the observations of 13 extended 3 CR quasars by Bridle *et al.* (1994), in which all 13 objects have unambiguous jets according to the same quantitative criteria, and seven counterjet candidates were identified. The quasars also exhibited a pronounced asymmetry in their lobes: hot spots were detected in every jetted lobe, but in only eight of the counterjet lobes. The difference in jet detection between the 13 QSRs and the first 5 RGs is consistent with unifying the two source classes using the relativistic-beaming model.

This paper reports new observations of 3C 20, 3C 34, 3C 42, 3C 244.1, 3C 252, 3C 325, 3C 330, and 3C 441 and 5 GHz with the VLA's *A* and *B* configurations. This completes the RG observations, so that an analysis paralleling that for the QSRs can now be undertaken in terms of the jet/counterjet flux density ratios, the compact central feature prominence, and the hot spots.

Section 2 briefly describes the selection of the radio galaxies, and our observing and imaging techniques. Section 3 describes each source individually. Section 4 discusses the prominence of the compact central features and jets, and the asymmetries in the hot spots and lobes of the radio galaxies and quasars. Section 5 discusses our overall results and their implications for Barthel's unification model.

Throughout this paper, we use $H_0 = 100$ km/s/Mpc, $q_0 = 0.5$, and assume a Friedmann–Robertson–Walker cosmology.

2. RADIO OBSERVATIONS

2.1 Sample

The selection criteria of the 3CR radio-galaxy sample are: (a) declination $20° \leqslant \delta < 70°$; (b) redshift $0.3 < z < 1.4$; (c) integrated flux density $S_{178\ \mathrm{MHz}} > 10$ Jy; and (d) largest angular size $10'' \leqslant \mathrm{LAS} < 100''$. This sample was chosen to match the criteria in the quasar sample of Bridle *et al.* (1994).

Table 1 lists the radio properties of all 13 radio galaxies. Table 2 gives the total integration times and bandwidths for the eight sources observed in the second round. Table 3 lists the primary and secondary calibrators used in the 5 GHz observations, with their flux densities and positions.

2.2 Comparison of the RG and QSR samples

The 13 RGs have angular sizes from $10''$ (3C 324) to $78''$ (3C 265), redshifts from 0.174 (3C 20) to 1.2 (3C 324), and luminosities from $10^{26.1}$ (3C 20) to $10^{27.1}$ W/Hz (3C 324). The average values for the angular size, redshift, and luminosity are $47\overset{''}{.}3$, 0.73, and $10^{26.7}$ W/Hz, respectively for the RGs. For the 13 QSRs, the angular sizes are from $14''$ (3C 9) to $79''$ (3C 47), the redshifts from 0.31 (3C 249.1) to 2.01 (3C 9), and the luminosities from $10^{26.0}$ (3C 249.1) to $10^{27.6}$ (3C 9), with average values of $45\overset{''}{.}3$, 0.9, and $10^{26.7}$ W/Hz, respectively. The two samples have approximately the same angular size and luminosity averages. The average redshift of the RGs is somewhat smaller than that of the QSRs, due to a revised redshift of the RG 3C 20 (see Sec. *3.1* below).

Figure 1 shows normalized histograms for redshift z, largest angular size LAS, and luminosity L. A Kolmogorov–Smirnov test shows the three distributions to be similar at the 96% significance level for the angular size, but only at the 62% significance level for both the redshift and the luminosity. The low significance level for the redshift and luminosity was expected in light of the above discussion.

TABLE 3. VLA 5 GHz calibrators.

Source	Calibrator	α(1950) hh mm ss.ss	δ(1950) dd mm ss.ss	Flux Dens. (Jy)
3C 20 3C 34	0133+476	01 33 55.10	47 36 12.86	1.88
3C 42 3C 441	0026+346	00 26 34.83	34 39 57.71	1.85
3C 244.1	1031+567	10 31 55.95	56 44 18.17	1.22
3C 252	1128+385	11 28 12.51	38 31 51.62	1.10
3C 325 3C 330	1642+690	16 42 18.06	69 02 13.22	1.60
3C 286	1328+307	13 28 49.66	30 45 58.64	7.5
3C 48	0134+329	01 34 49.83	32 54 20.52	5.60
3C 138	0518+165	05 18 16.53	16 35 26.9	4.0

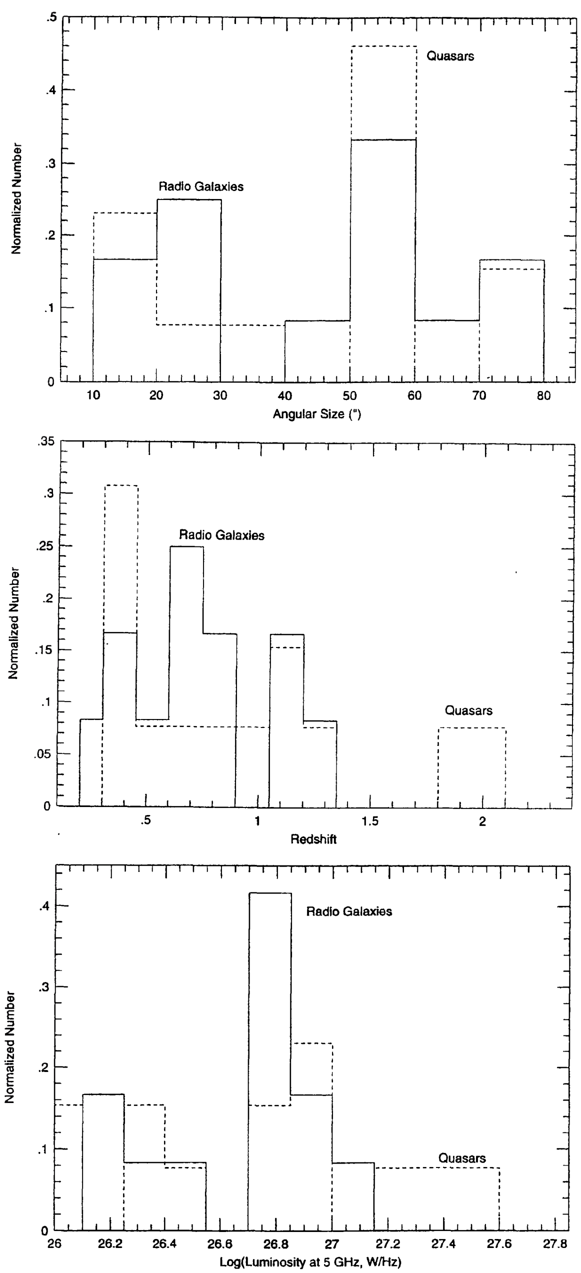

FIG. 1. Distribution of the angular size, redshift, and total luminosities for the 13 radio galaxies and the 13 quasars of Bridle *et al.* (1994a).

2.3 *Observing and Imaging Techniques*

The observing strategy discussed by Fernini *et al.* (1993) was used for the eight radio galaxies listed in Table 2. Typical integration times for each source for the *A* and *B* configurations were 2.7 and 1.4 hours, respectively. The rms sensitivity is thus typically about a factor of 1.5 worse than that of Bridle *et al.* (1994) for the quasars, but dynamic ranges are generally similar. The *A* and *B* configuration data were calibrated following standard procedures (e.g., Fomalont & Perley 1989) using the NRAO's AIPS software. The data from each configuration were initially Fourier transformed and deconvolved separately using the ungridded-subtraction CLEAN algorithm (AIPS task MX), to obtain input models for phase and amplitude self-calibration (AIPS task CALIB). Before adding the *A* and *B* configuration *uv* data, the latter were weighted to produce the same brightness sensitivity as the *A* configuration data on the final images and to minimize the effects of beam skirts.

TABLE 4. RMS noises (μJy) and dynamic ranges for the $(A+B)$ 5 GHz maps.

	3C 20	3C 34	3C 42	3C 244.1	3C 252	3C 325	3C 330	3C 441
I (rms/beam)	70(30)	28(25)	22(18)	45(25)	20(20)	30(20)	47(25)	36(20)
Q,U (rms/beam)	45	15	27	29	25	26	36	22
Dynamic Range	3250:1	300:1	2500:1	6300:1	2500:1	6500:1	6800:1	2000:1

Table 4 lists the parameters of the final images. The theoretical noise is reported in parentheses beside the measured rms noise. Contour maps of these eight radio galaxies are presented in Figs. 2–24.

3. THE IMAGES

In order to quantify the features seen on high resolution images, Fernini *et al.* (1993) and Bridle *et al.* (1994) used specific definitions when identifying the "compact central feature," "jet," "lobes," and "hot spot." For consistency, the same definitions are used here:

(1) Compact central feature—a central unresolved feature coinciding to within observational errors with the best available position for the optical galaxy.

(2) Jet—a narrow feature that is (a) at least four times as long as it is wide (after deconvolving the synthesized beam), (b) separable at high resolution from other extended structure either spatially or by brightness contrast, and (c) aligned with the nucleus of the parent object where it is closest to it.

(3) Lobes—features which contain all of the other radio emission produced by the source excluding (1) and (2).

(4) Hot Spot—if no jet is detected, a feature that (a) is the brightest structure in the lobe, (b) has surface brightness more than four times that of the surrounding emission, and (c) has a linear FWHM (after deconvolving the synthesized beam) that is <5% of the largest diameter of the source. If a jet is detected, the hot spot must additionally be further from the nucleus than the end of the jet, which is defined by (1) its disappearance, or (2) an abrupt change in direction by at least 30°, or (3) decollimation by more than a factor of 2. As it will be seen below, some of our RGs do not show any hot spots according to this definition for the following two reasons: (1) the lobes were so well resolved that no feature qualified as a hot spot, or (2) there are several bright hot spot candidates, but they were not well enough resolved for us to be able to tell which is the hot spot.

3.1 *3C 20*

3C 20 was originally included in our sample on the basis of the redshift of 0.350 given by Spinrad *et al.* (1985). More recently, Laing (private communication) reported $z=0.174$ based on both strong emission lines and stellar absorption

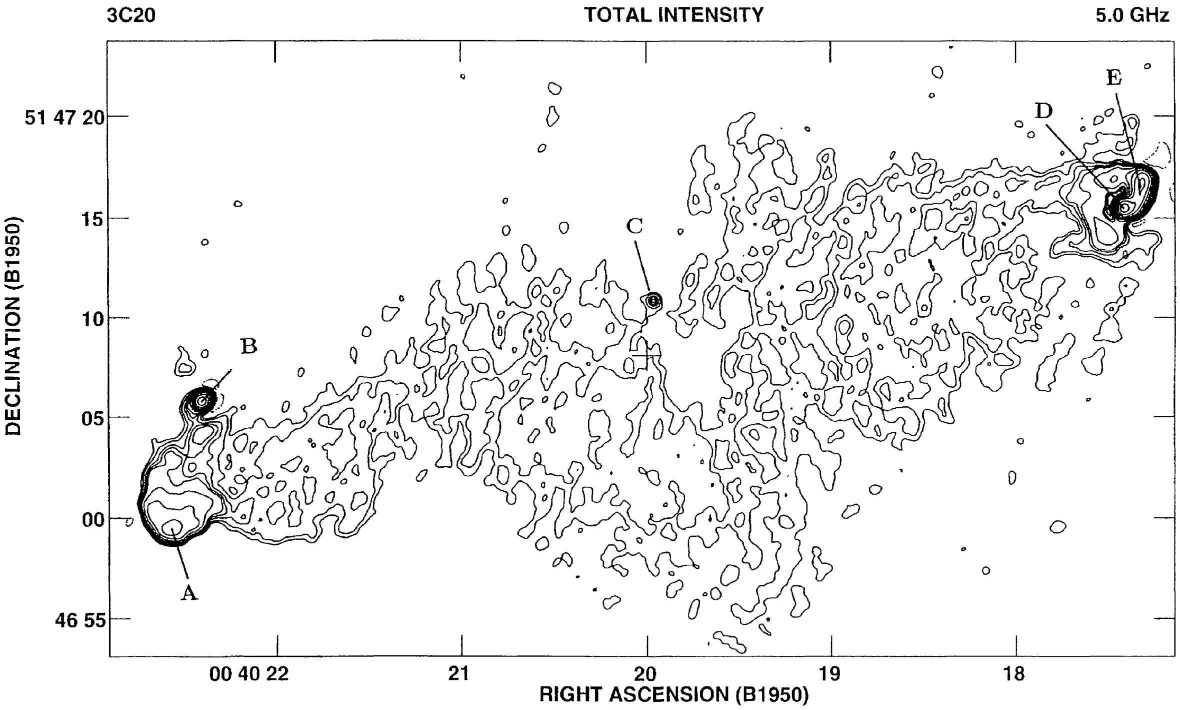

FIG. 2. Contour map of the total intensity of 3C 20 at 5 GHz with 0."43 resolution from the combined *A* and *B* configuration data. B and D are the hot spots. The plus sign, here and in all other figures, below the feature C indicates the position of the optical nucleus. Contours are drawn at −2 (dotted), 1, 2, 4, 6, 8, 16, 32, 64, 128, 256, 512, and 1024 times 284 μJY per CLEAN beam area. The peak intensity is 228 mJy per CLEAN beam area.

features in the spectrum (Lawrence *et al.* 1986). Thus, 3C 20 is actually below the redshift cutoff for our sample, but we retain it here for completeness.

Previous VLA images (Laing 1982; Hiltner *et al.* 1994) of this double-lobed radio galaxy show a bright "hot spot" in the western lobe which at subarcsecond resolution is separated into a southern compact feature D with a tail to the north, and which ends in a secondary intensity peak E. On the eastern side, the lobe consists of a double structure, formed by a compact feature B in the north and an asymmetric, edge-brightened region to the south A.

Figure 2 shows our total intensity image at 0."43 resolution from the *A* and *B* configuration data. The structure is about 51" in extent with symmetrically placed and very diffuse lobes of emission. The compact central feature C coincides with the optical identification proposed by Spinrad *et al.* (1985) to within 0."1. The radio properties of this feature and those of the other RGs are listed in Table 5. The compact central radio feature of 3C 20 was first reported by Hiltner *et al.* (1994). The "+" seen on this and other maps indicates the position of the optical nucleus.

The southeast lobe contains a strong compact component B (peak flux density of 125.1 mJy) that is recessed from the outer edge of the lobe and from the less well-defined boundary feature A. Feature B has a higher surface brightness than A at this resolution, and meets our criterion for being the hot spot in this lobe.

Two distinct feature D and E are contained in the western lobe. Besides being more compact, feature D has a higher surface brightness than E and hence qualifies as the hot spot.

TABLE 5. Parameters of the compact central features.

Source	α(1950) h m s	δ (1950) ° ′ ″	Peak S_{5GHz} (mJy)	Log(L_{5GHz}) (W/Hz)	Size (max × min.)	p
3C 20	r 00 40 19.963 o 00 40 20.08	51 47 10.90 51 47 10.2	2.6 (0.2)	22.9	0."33 × 0."20	< 0.08
3C 22*	r 00 48 4.731 o 00 48 4.71	50 55 44.80 50 55 45.4	7.3 (0.6)	24.9	0."09 × 0."03	< 0.01
3C 34	r 01 07 32.572 o 01 07 32.51	31 31 22.60 31 31 21.9	0.40 (0.03)	23.4	0."22 × 0."08	< 0.05
3C 42	r 01 25 42.659 o 01 25 42.68	28 47 30.30 28 47 30.4	2.4 (0.1)	23.6	0."23 × 0."13	< 0.01
3C 55	r 01 54 19.055 o 01 54 19.03	28 37 2.80 28 37 00.6	5.0 (0.3)	24.6	0."06 × 0."03	< 0.05
3C 244.1	r 10 30 19.582 o 10 30 19.75	58 30 4.40 58 30 05.2	1.8 (0.1)	23.6	0."19 × 0."14	< 0.08
3C 252	r 11 08 48.846 o 11 08 48/93	35 56 59.90 35 57 00.1	2.2 (0.2)	24.6	0."3 × 0."17	< 0.02
3C 265	r 11 42 52.353 o 11 42 52.39	31 50 26.60 31 50 29.1	2.7 (0.7)	24.4	< 0."13	< 0.06
3C 324	r — — —.— o 15 47 37.10	— — —.— 21 34 40.1				
3C 325	r 15 49 13.963 o 15 49 13.99	62 50 21.20 62 50 20.0	2.4 (0.2)	24.3	0."2 × 0."05	< 0.07
3C 330	r 16 09 14.077 o 16 09 13.90	66 04 22.60 66 04 22.3	0.74 (0.04)	23.4	0."22 × 0."12	< 0.01
3C 356	r 17 23 06.954 o 17 23 06.66	51 00 14.20 51 00 18.2	1.1 (0.1)	24.3	< 0."13 (D) < 0."20 (E)	< 0.06
3C 441	r 22 03 49.204 o 22 03 49.27	29 14 45.70 29 14 43.8	3.5 (0.5)	24.4	1."25 × 0."82	< 0.03

Notes to Table 5

p: fractional polarization (or 3σ upper limit) at position of peak
*: 3C 22 shows a quasar-like nucleus (Economou *et al.* 1995).

TABLE 6. Jet/counterjet flux densities for the sample of 13 RGs.

	Straight Path			Whole Path	
Source	Flux Dens. (mJy)	$\log(L_{5GHz})$ (W/Hz)	Length (″)	Flux Dens. (mJy)	Length (″)
3C 20	NW < 1.34	22.6	20.6	< 70.3	23.7
	SE < 0.21	21.8	20.6	< 36.4	23.7
3C 22*	NW 1.72(0.15)	24.2	3.6	8.06(0.31)	11.8
	SE < 0.085	22.9	3.6	5.56(0.07)	8.4
3C 34	W < 0.06	22.5	18.4	< 24.2	21.2
	E < 0.06	22.5	18.4	< 6.3	21.2
3C 42	NW < 0.07	22.1	11.5	< 7.5	11.7
	SE < 0.07	22.1	11.5	< 17.2	14.5
3C 55	E < 0.07	22.6	28	< 49	31.5
	W < 0.64	23.6	28	< 6.1	30.8
3C 244.1	NW < 0.05	22.0	17.5	< 7.2	25
	SE < 0.14	22.5	17.5	< 0.4	17.3
3C 252	W < 0.06	22.9	17	< 4.4	37.1
	E < 0.06	22.9	17	< 8.9	20
3C 265	NW < 0.07	22.7	14	< 13.3	45
	SE < 0.07	22.7	14	< 4.5	28.2
3C 324	SW < 0.09	23.2	2.2	< 1.2	3.5
	NE < 0.09	23.2	2.2	< 1.2	4.6
3C 325	NW < 0.85	23.9	3.3	< 10.2	7.9
	SE < 0.18	23.2	3.3	< 41.2	6.9
3C 330	SW < 0.14	22.7	27.5	< 66.3	30
	NE < 0.14	22.7	27.5	< 29.3	27.1
3C 356	NW < 1	24.1	4.4	< 22.5	43.8
	SE < 0.1	23.1	4.4	< 6.2	22.9
3C 441	NW 7.6(0.2)	24.6	6.3	5.3(0.2)	7.5
	SE < 0.11	22.8	6.3	< 31.2	26.2

Note to Table 6

*: 3C 22 shows a quasar-like nucleus (Economou *et al.* 1995).

It is also the site of polarized optical, presumably synchrotron, emission reported by Hiltner *et al.* (1994).

There are no jet or counterjet candidates in 3C 20. A marginal elongated structure on the north rim of the western lobe does not fit our jet definition.

Both lobes of 3C 20 have diffuse emission extending toward the compact central feature, and bending toward the south. The two hot spots B and D are aligned to within 2° across the compact central feature. D is marginally (about 5%) less compact than B, but is clearly brighter than D due to a factor ~2 in intensity. (Table 7 gives the fitted sizes and flux densities of all features reported on these images).

Figure 3 shows the polarized emission over the eastern lobe and the compact central feature, and Fig. 4 shows the polarized emission over the western lobe. The lengths of the vectors overlaid on the intensity contours in the polarization displays for these and the other sources are proportional to the fractional polarization and their position angles are those of the E vectors. We show no polarization data below a signal-to-noise ratio of 4:1.

The two lobes of 3C 20 are symmetrically polarized (40% on average). The edges of both lobes are highly polarized (41%–48%) with the E vectors perpendicular to the local ridge lines. The averages for the polarization were computed using $\Sigma P/\Sigma I$.

3.2 3C 34

At 20 cm and at 2″ resolution, Johnson *et al.* (1995) reported a double "hot spot" in the western lobe and a single "hot spot" in the eastern lobe of 3C 34. They also found evidence for jets on both sides of 3C 34 at both 1.4 and 5 GHz, and for a depolarization "silhouette"—a region of stronger local depolarization. The silhouette is believed to be caused by another galaxy in the same cluster as the radio galaxy. Some extended emission-line gas overlaps with the radio lobes of 3C 34. Johnson *et al.* (1995) concluded that the only clear effect on the radio polarization is that in one region depolarization is almost total even at λ6 cm; elsewhere the gas may lie behind the radio emission.

Figure 5(a) shows our total intensity contours at 0.″5 resolution from the A and B configuration data. The lobes are 48″

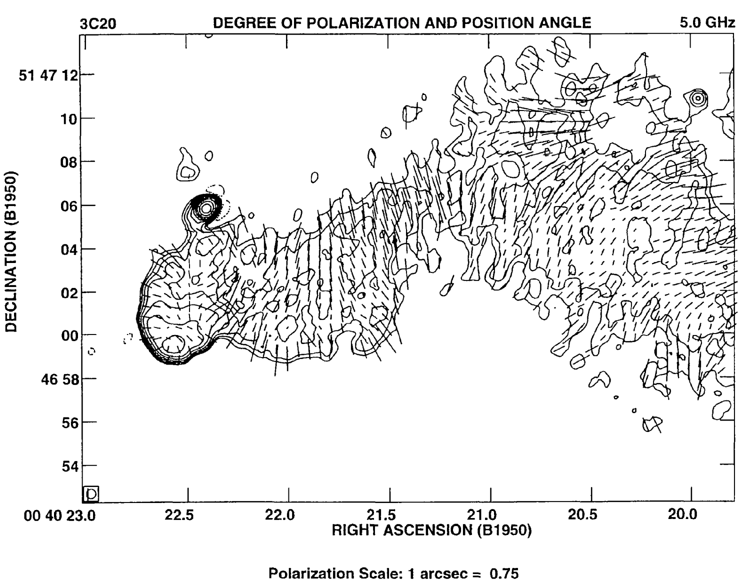

FIG. 3. Enlargement of the eastern lobe of 3C 20 and its distribution of the degree of linear polarization and E-vector position angle at 5 GHz, superposed on contours from Fig. 2. A vector length of 1″ corresponds to $p=0.75$.

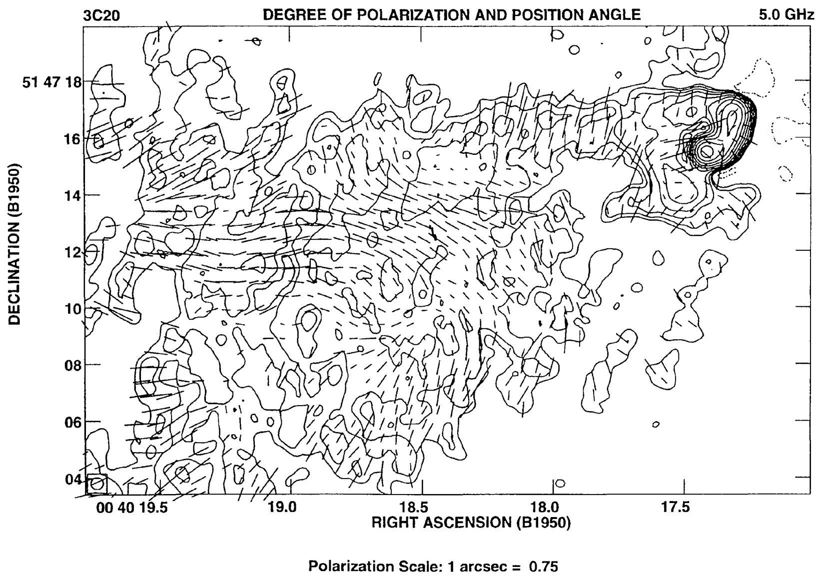

FIG. 4. Enlargement of the western lobe of 3C 20 and its distribution of the degree of linear polarization and E-vector position angle at 5 GHz, superposed on contours from Fig. 2. A vector length of 1″ corresponds to $p=0.75$.

across and symmetrically placed with respect to the compact central feature E. The optical nucleus and E coincide within the positional errors reported by Laing *et al.* (1983).

Several features can be seen on the eastern lobe (A, B, C, D) and on the western lobe (F, G). The extended features C and D might be parts of a jet candidate with feature D being more elongated toward the compact central feature, but they do not meet our definition. Our 5 GHz B configuration image [Fig. 5(b)] at 1.″2 resolution shows a "jet-like" structure similar to that of Johnson *et al.* (1995) linking the compact central feature to the western lobe. However, our image of 3C 34 at 0.″5 resolution does not show this structure as a jet. This might just be some extended emission from the western lobe.

On the outer edge of the eastern lobe the features A and B were fitted with two-dimensional Gaussians. Feature B is more compact than A, but its surface brightness is not four times that of the surrounding region so it does not qualify as a hot spot by our definition. On the western lobe, feature G is elongated toward an extended feature H on the northern outer edge of this lobe. A Gaussian fit of F and G shows F as being more compact than G. Feature F, however, fails the surface brightness requirement to be a hot spot.

Figures 6 and 7 show polarization maps with E vectors overlaid on the eastern and western lobe of 3C 34, respectively. The average degrees of linear polarization for the eastern and western lobes are 36% and 39%, respectively.

3.3 3C 42

A previous 20 cm VLA image of 3C 42 (Leahy & Perley 1991) at 1.″2 resolution shows two lobes with a bridge of emission between them. At this resolution, no compact central feature was detected. Figure 8 shows our total intensity contours of 3C 42 at 5 GHz with 0.″41 resolution. The source has two extended lobes with emission that extends back nearly to the (newly detected) compact central feature B. This feature coincides with the optical identification of Spinrad *et al.* (1985).

The NW lobe includes two compact features C and D at its outer edge and a large collimated bridge. The edges of this bridge are well-defined, and it transverse intensity profile is flat-topped, but following our jet definition this bridge is too wide to be considered a jet. The most compact feature C has a peak brightness of 62.1 mJy. It has all the characteristics of a hot spot. In the SE lobe, feature A has the required compactness, but not the surface brightness of a hot spot. This feature aligns with B and feature D to within 5°.

Figure 9, also at 0.″41 resolution, shows the polarization data. The average degree of linear polarization of the NW and SE lobes are 36% and 32%, respectively. Hot spot C is 19% linearly polarized at the peak. The edges of the SE lobe are more polarized (34%) than the edges of the NW lobe (18%). The polarization of the northern and southern ridges of the bridge are quite high (47%) with E vectors perpendicular to the ridge lines.

3.4 3C 244.1

A previous 20 cm VLA image of 3C 244.1 by Alexander & Leahy (1987) showed two radio lobes with an angular separation of 51″, but with no compact central feature or jet. Our 5 GHz image at 0.″41 resolution from the combined *A* and *B* configuration data is shown in Fig. 10. This source has asymmetric-placed lobes with respect to the compact central feature D, but equally bright lobes. The compact central feature D detected here for the first time coincides with the optical identification of Spinrad *et al.* (1985) to within the positional errors given by Laing *et al.* (1983).

The size fitted to the bright recessed feature C in the south lobe about 2/3rds of the way out from the compact central feature is about 0″.45×0″.41 (Table 6). It is not extended enough to qualify as part of a jet.

There are two hot spot candidates A and B at the outer edges of the southern lobe, and one recessed candidate C. Feature A is noticeably more compact than B, but does not satisfy our surface brightness requirement for a hot spot. We tentatively classify C as the hot spot. There is no evidence of a counterjet on the northern side of the source beside the bright feature E, which fits our definition of a hot spot.

Figures 11 and 12 plot the polarization data on contours from Fig. 10 for the southern and northern lobes, respectively. The average degrees of linear polarization are respectively 38% and 40%. The highest degrees of polarization (42%–56%) occur near the edges of the lobes. The bright feature C has about 43% polarization at the peak. The polarization at the peak of hot spot E is about 9%.

3.5 3C 252

A previous 5 GHz VLA image of 3C 252 by Leahy & Williams (1984) showed two distinct lobes with no compact central feature or jet. Figure 13 shows our 5 GHz total intensity image at 0″.4 resolution from the combined *A* and *B* configuration data. This large (57″) source shows no jet or counterjet candidate.

The lobes of this radio source have less extended emission in comparison to the lobes of the other radio galaxies in this sample and are unusually asymmetric about the compact central feature D which we have detected for the first time. The position of the compact central feature agrees to within 0″.1 with the optical identification of Spinrad *et al.* (1985).

Features A and B may be parts of a ridge that is nearly perpendicular to the line between A and C. As feature C is brighter and more compact than A or B, we classify C as the hot spot. The NW lobe contains one bright feature E elongated toward the northern edge of the lobe. Due to its compactness and high surface brightness, E is the hot spot of the NW lobe. The two hot spots of this source, C and E, and the compact central feature are aligned to within 8°.

Figures 14 and 15 plot the polarization data for the SE and NW lobes, respectively. The average degrees of linear

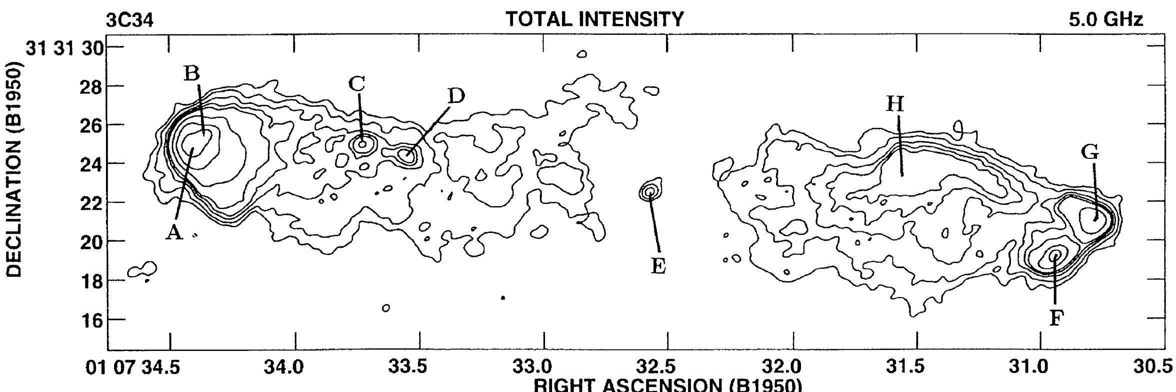

(a)

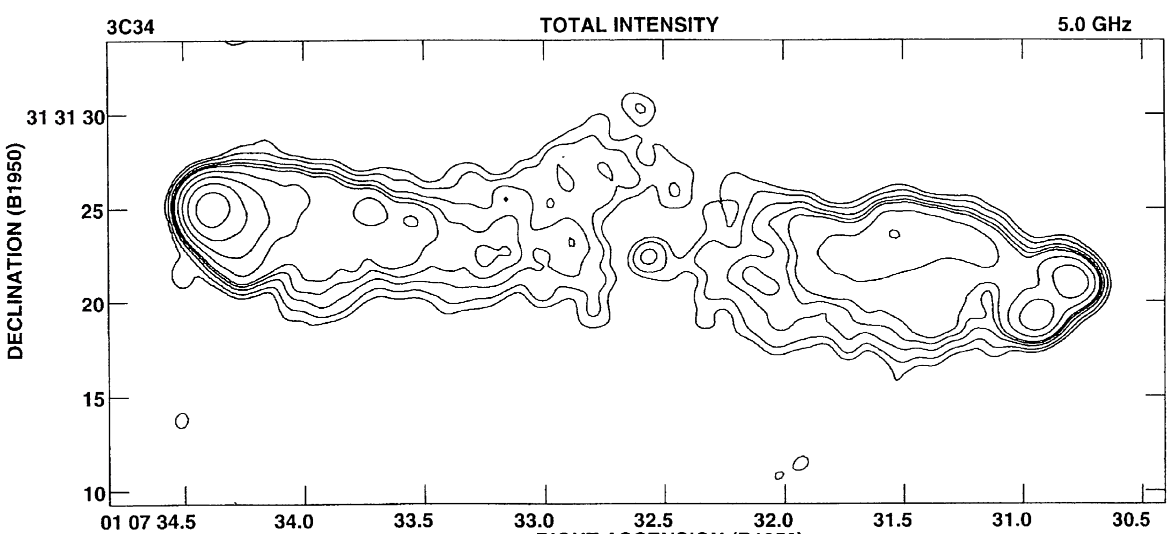

(b)

FIG. 5. (a) Contour map of the total intensity of 3C 34 at 5 GHz at 0″.50 resolution from the combined *A* and *B* configuration data. Contours are drawn at −2 (dotted), 1, 2, 4, 6, 8, 16, 32, 64, 128, 256, 512, and 1024 times 84 μJy per CLEAN beam area. The peak intensity is 8.7 mJy per CLEAN beam area. (b) Contour map of the total intensity of 3C 34 at 5 GHz at 1″.2 resolution from the *B* configuration data. Contours are drawn at −2 (dotted), 1, 2, 4, 6, 8, 16, 32, 64, 128, 256, 512, and 1024 times 150 μJy per CLEAN beam area. The peak intensity is 30 mJy per CLEAN beam area.

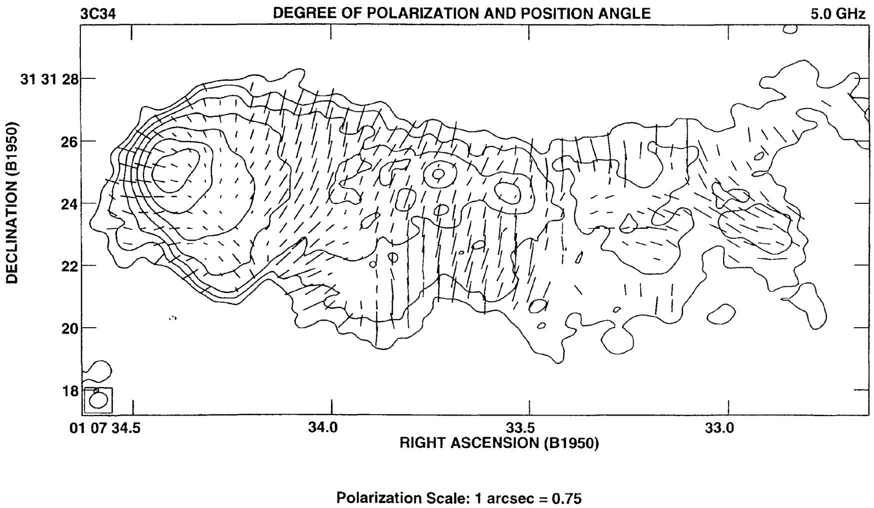

FIG. 6. Contour map of the total intensity of the eastern lobe of 3C 34 and its distribution of the degree of linear polarization and E-vector position angle at 5 GHz, superposed on contours from Fig. 5. A vector length of 1″ corresponds to $p=0.75$.

polarization are 44% and 38% for the SE and NW lobes, respectively. The polarizations at the peak of hot spot C and E are 32% and 5%, respectively.

3.6 3C 325

Figure 16 shows our 5 GHz total intensity image at 0.″4 resolution from the combined *A* and *B* configuration data. This small (16″) source has asymmetrically-placed lobes. The two elongated features F and E may be part of a jet candidate. The diffuse feature E lies on the likely path of any putative jet, but it is broad and round, and may simply be the brightest part of a diffuse lobe structure in this region.

The optical position for the nucleus of 3C 325 (Table 5) is within 0.ˢ025 in α and 1.″20 in δ of the radio compact central feature D, detected here for the first time. The accuracy of the optical position (Laing *et al.* 1983) is 0.ˢ13 in α and 1.″0 in δ, so the identification is confirmed by our detection. R. Laing (private communication) recently tentatively classified the spectrum of this object as quasar-like on the basis of its appearance on the plates taken by Laing *et al.* (1978). Spinrad *et al.* (1985) classified 3C 325 as an N-galaxy and noted it optical appearance as compact. However, pending further optical studies, we will retain 3C 325 in our sample of RGs.

In the SE lobe, feature C is part of a ridge that extends from C to feature B. We consider this ridge to be a counterjet candidate. Features A and B are part of an elongated structure roughly perpendicular to the ridge. Our resolution is inadequate to say whether A or B better meets our definition of a hot spot. In the NW lobe, the bright and compact feature H meets all our requirements for being termed a hot spot.

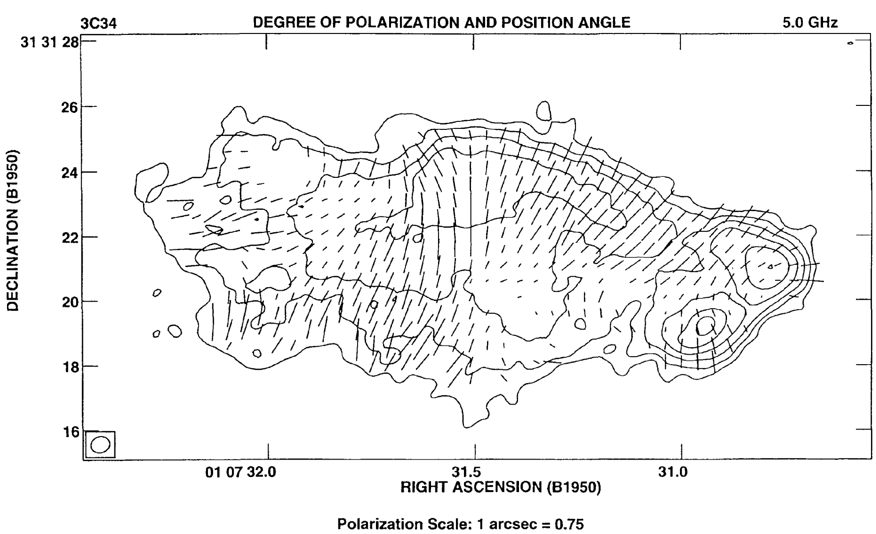

FIG. 7. Contour map of the total intensity of the western lobe of 3C 34 and its distribution of the degree of linear polarization and E-vector position angle at 5 GHz, superposed on contours from Fig. 5. A vector length of 1″ corresponds to $p=0.75$.

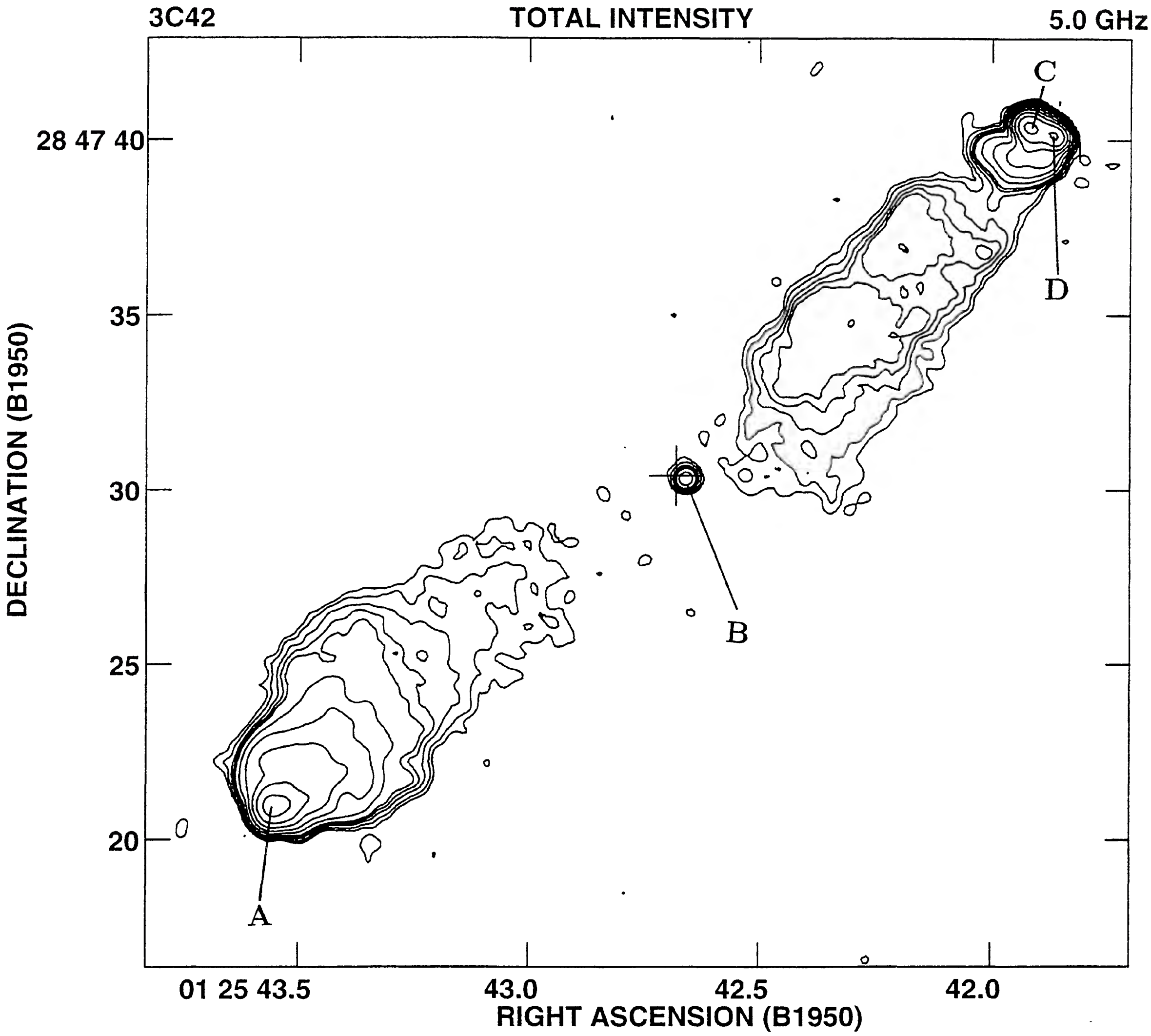

FIG. 8. Contour map of the total intensity of 3C 42 at 5 GHz with 0.″41 resolution from the combined *A* and *B* configuration data. C is the hot spot. Contours are drawn at −2 (dotted), 1, 2, 4, 6, 8, 16, 32, 64, 128, 256, 512, and 1024 times 88 μJy per CLEAN beam area. The peak intensity is 54 mJy per CLEAN beam area.

Feature B, hot spot H, and the compact central feature D are aligned to within 10°. The above ridge and feature C are offset north of this axis by about 5°.

Figure 17 plots the polarization data superposed on contours from Fig. 16. The diffuse feature E has 50% linear polarization, while feature F has <7% polarization at its peak. The *E* vectors are nearly perpendicular to the radio source axis from F through G. On the SE lobe, the *E* vectors are generally perpendicular to the lobe edges. The average degrees of linear polarization of the NW lobe without the diffuse feature F and the SE lobe are 20% and 28%, respectively.

3.7 3C 330

Figure 18 shows a 5 GHz total intensity image at 0.″43 resolution from the combined *A* and *B* configuration data. This source is 57″ in extent and has two compact, symmetrically placed lobes of equal brightness. Figures 19 and 20 show details of the NE and SW lobes. Both lobes show evidence of filaments.

We detected the weak compact central feature of 3C 330 for the first time. Its peak is 0.74 mJy at $\alpha = 16^h09^m14.^s081$ and $\delta = 66°04'22.''60$,within $0.^s181$ in α and 0.″3 in δ of the optical identification proposed by Spinrad *et al.* (1985). This confirms the identification.

The brightest regions of both lobes show internal structure that is not well enough resolved to apply our hot spot criteria unambiguously. The SW lobe contains two distinct feature, D and E, neither of which clearly meets our criterion, though E is both brighter and more compact at this resolution. Feature A in the NE lobe does not meet all our criteria, and its surroundings show signs of significant substructure. Higher resolution is required to confirm it as the hot spot. We note that the axis through feature A and feature D crosses the compact central feature, but the axis through the A and E

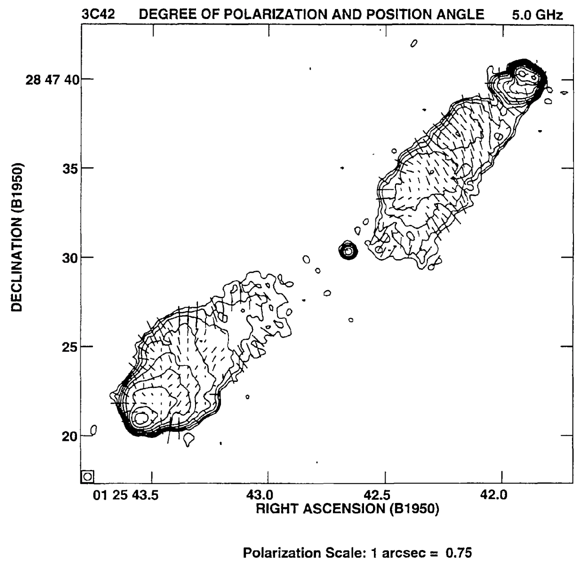

FIG. 9. Contour map of the total intensity of 3C 42 and its distribution of the degree of linear polarization and E-vector position angle at 5 GHz, superposed on contours from Fig. 8. A vector length of 1″ corresponds to $p=0.75$.

does not; the two axes are misaligned by about 3°. There are no signs of a jet or a counterjet.

Figures 21 and 22 plot the polarization of the NE and SW lobes at 5 GHz with polarization E vectors overlaid. The polarized radio emission appears to be evenly distributed in both lobes (32%).

3.8 3C 441

A previous 5 GHz VLA image of 3C 441 (Laing 1988) shows a jet linking a "knot" to the northern lobe. The identification of the knot with the compact central feature of the source is unclear (e.g., Garrington *et al.* 1991).

A 0.″38 resolution contour map of the total intensity at 5 GHz from the combined A and B configuration data is shown in Fig. 23. The optical position for the nucleus of 3C 441 is within 0.ˢ071 in α and 1.″90 in δ of feature C. The positional errors of Laing *et al.* (1983) are 0.ˢ07 in α and 1.″0 in δ. If feature C represents the actual compact central feature of 3C 441, there is a positional discrepancy in δ between it and the optical nucleus.

There is a definite jet between feature C and the NW lobe. The jet contains no strong knots (besides C) and consists of a fairly short bridge of emission between C and D.

Feature D in the NW lobe marks the end of the jet. This feature is compact and has a high surface brightness in comparison to its surroundings, so we identify it as the jetted hot spot. Two more diffuse features E and F lie beyond this hot spot.

The SE lobe is less extended than the NW lobe, with a bright rim on its northern edge. This rim starts just after the bright feature A and goes along the northern ridge of the lobe until it reaches feature B.

Figure 24 shows the polarization data on contours from Fig. 22. The degree of the linear polarization of the jet varies between 10% and 25% from the NW outer limits of C to D. The highest degrees of polarization (23%–42%) occur near the edges of both lobes. The E vectors are roughly perpendicular to the lobe boundaries.

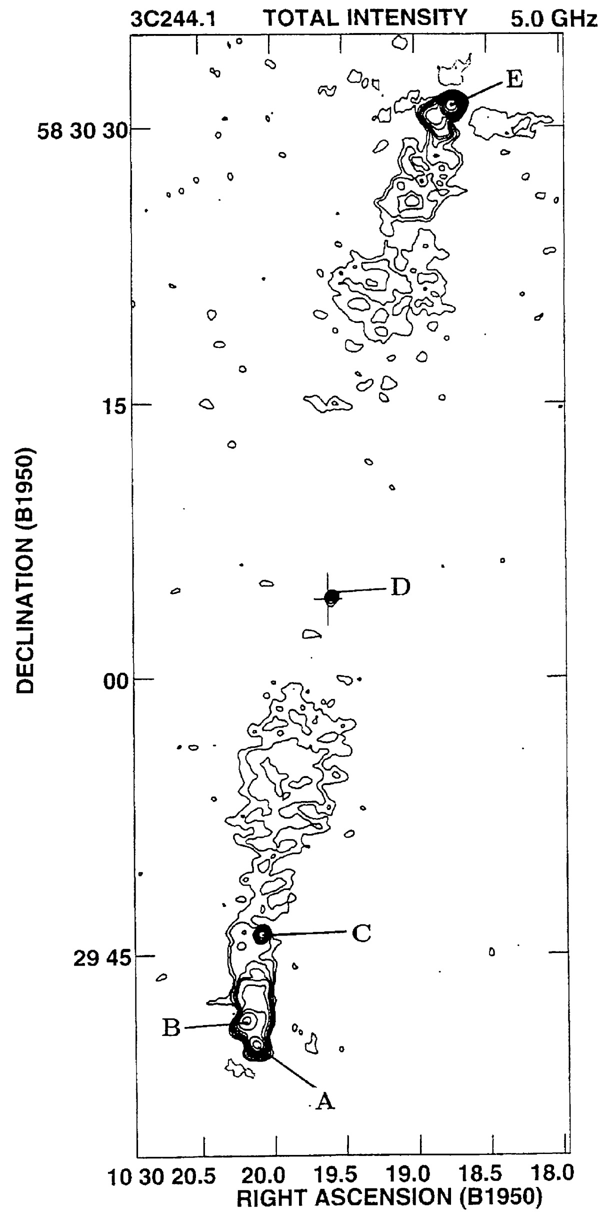

FIG. 10. Contour map of the total intensity at 5 GHz of 3C 244.1 with 0.″41 resolution from the combined A and B configuration data. Features C and E represent the two hot spots. Contours are drawn at −2 (dotted), 1, 2, 4, 6, 8, 16, 32, 64, 128, 256, 512, and 1024 times 200 μJy per CLEAN beam area. The peak intensity is 219 mJy per CLEAN beam area.

4. PARAMETERS OF THE MAJOR FEATURES

4.1 Compact Central Features

Table 5 lists the observed parameters of the compact central features of the 13 FR II radio galaxies, as fitted by two-dimensional Gaussian models within small regions around

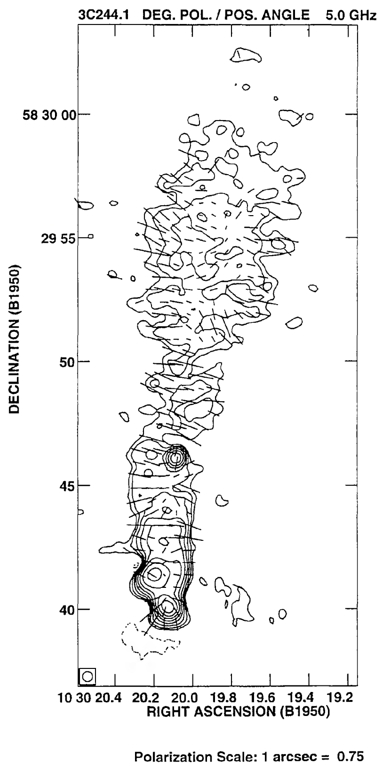

FIG. 11. Contour map of the total intensity of the southern lobe of 3C 244.1 and its distribution of the degree of linear polarization and E-vector position angel at 5 GHz, superimposed on contours from Fig. 10 but times 180 μJy per CLEAN beam area. A vector length of 1″ corresponds to $p=0.75$.

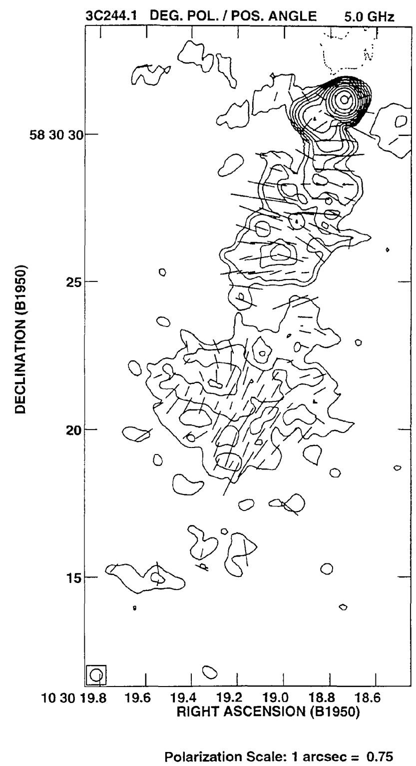

FIG. 12. Contour map of the total intensity of the northern lobe of 3C 244.1 and its distribution of the degree of linear polarization and E-vector position angle at 5 GHz, superposed on contours from Fig. 10 but times 180 μJy per CLEAN beam area. A vector length of 1″ corresponds to $p=0.75$.

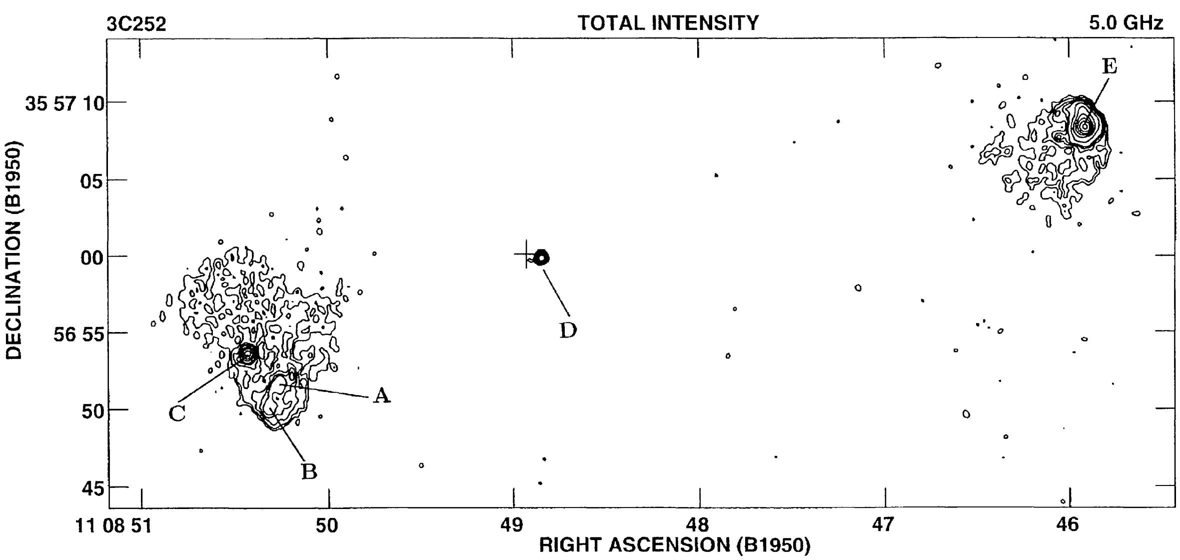

FIG. 13. Contour map of the total intensity of 3C 252 at 5 GHz from the combined A and B configuration data at 0″.4 resolution. Features C and E represents the two hot spots. Contours are drawn at −2 (dotted), 1, 2, 4, 6, 8, 16, 32, 64, 128, 256, 512, and 1024 times 80 μJy per CLEAN beam area. The peak intensity is 50 mJy per CLEAN beam area.

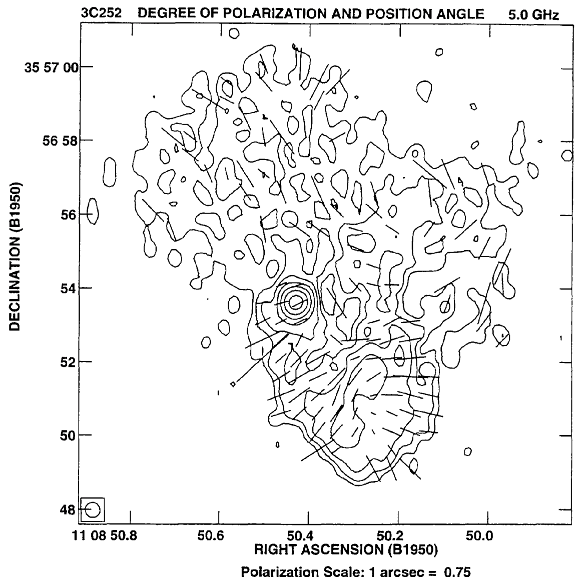

FIG. 14. Contour map of the total intensity of the SE lobe of 3C 252 and its distribution of the degree of linear polarization and E-vector position angle at 5 GHz, superposed on contours from the figure. A vector length of 1″ corresponds to $p=0.75$.

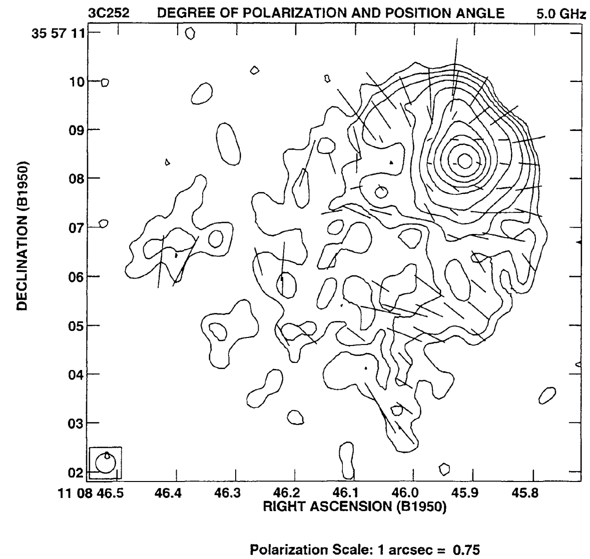

FIG. 15. Contour map of the total intensity of the NW lobe of 3C 252 and its distribution of the degree of linear polarization and E-vector position angle at 5 GHz, superposed on contours from the figure. A vector length of 1″ corresponds to $p=0.75$.

the peak intensity. The radio positions are those of the peak intensities of these features. The quoted flux densities are the peak flux densities. The size limits are the deconvolved maximum and minimum sizes as given by the AIPS task IMFIT.

Table 5 also gives positions for the optical identifications, from Laing *et al.* (1983) and Spinrad *et al.* (1985). With the exceptions of 3C 55, 3C 265, 3C 356, and 3C 441, the optical identification of the RGs are confirmed to within the positional errors of Laing *et al.* (1983).

The compact central features of the quasars are more luminous on average than those of the RGs. (Note that all thirteen quasar compact central features were detected, whereas only ten of the RG compact central features were detected, eight for the first time.) This previously known difference (Miley 1980; Bridle & Perley 1984) between the two types of object is illustrated in Fig. 25, which plots the compact central feature luminosity versus the total luminosity of the source, and in Fig. 26 which plots the ratio of the compact central feature to the total luminosity for our two samples. The K–S test shows that the two compact central feature distributions are statistically similar at only the 0.2% significance level. This is a clear distinction between the RGs and the QSRs, obviously in accord with the unification scheme of Barthel (1989).

Table 5 also lists the linear polarizations observed for the central features. Most of the values reported are upper limits (3σ).

4.2 *Jets and Counterjets*

We have detected a definite jet in only two RGs (3C 22 and 3C 441). However, since the publication of Paper I, Economou *et al.* (1995) reported the detection of a redshifted, broad Hα line in the near-IR in 3C 22, suggesting that this source has a quasar-like nucleus.

Candidate jets or jet components are present in 3C 34, 3C 55, 3C 265, 3C 324, and 3C 325. 3C 244.1 has a component C that may be either a recessed hot spot or a jet knot. In all cases, there is a strong possibility of confusion with lobe edge-brightening or filaments. The low (2 of 13) rate of unambiguous jet detection in the RG sample stands in strong contrast to the jet detection rate (13 in 13) in the QSRs of Bridle *et al.* (1994). The implication of these results are discussed in Sec. 5. Besides the low jet detection in the RGs, no counterjet has been seen for the thirteen RGs.

Table 6 lists integrated flux densities (mainly 3σ upper limits) for the jet and counterjet emission in each RG, together with the lengths (in arcseconds from the compact central feature) of the regions over which the integration was performed. The integrated flux densities were estimated by normalized pixel summation (AIPS task IMEAN) as follows. The images were rotated and regridded (AIPS task LGEOM) to make the initial segments of the jets, if any, or the main axis of the source, lie along rows or columns of the rotated maps. The measurements were confined to the regions opposite the compact central feature using two rectangular boxes of equal area. A mean background correction was determined from the same sized boxes on either side. Figure 27 shows a plot of the jet/counterjet luminosities for the RGs and the QSRs versus the compact central feature luminosities. As expected from the unified scheme, the RGs show weaker jets than the QSRs.

4.3 *Hot Spots*

Table 7 reports parameters for the hot spot candidates for our sample. We emphasize that the parameters in this table

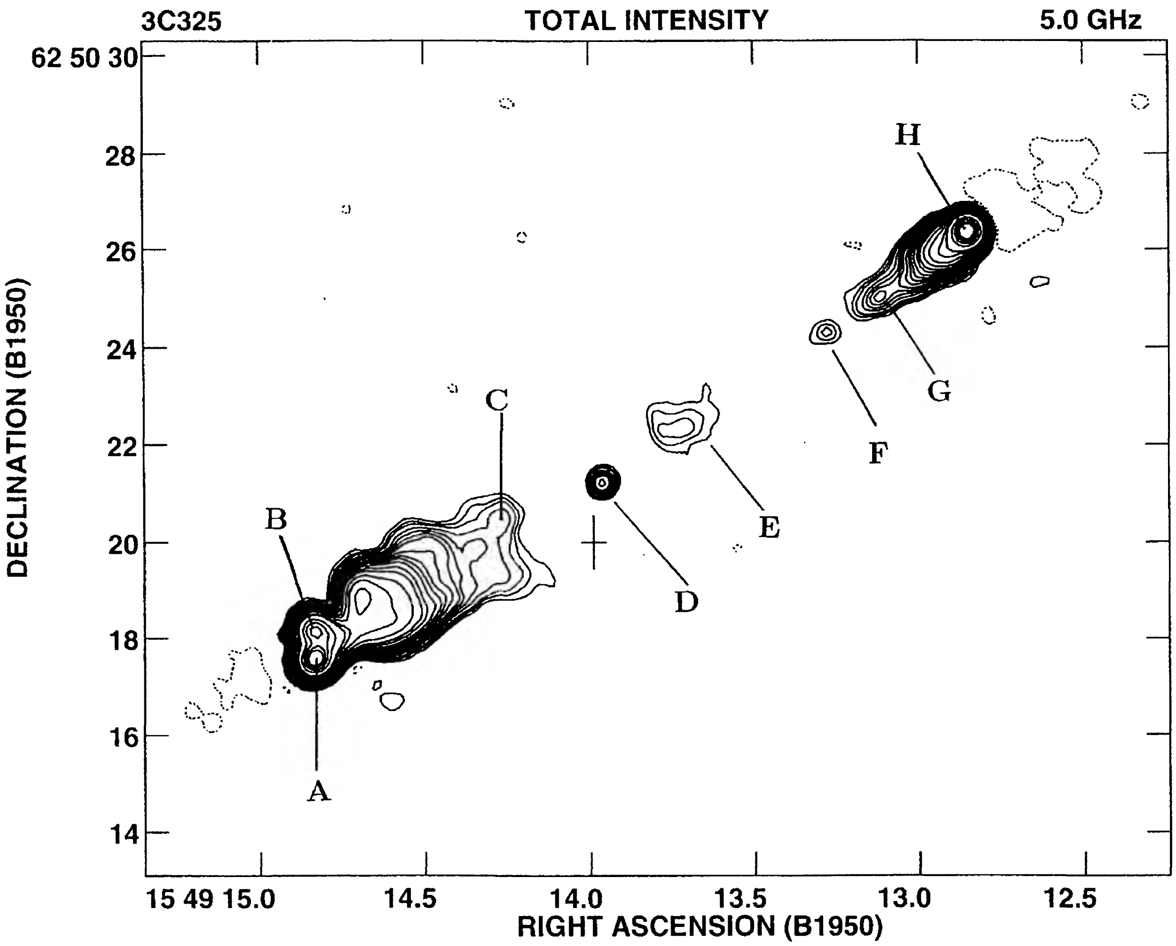

FIG. 16. Contour map of the total intensity of 3C 325 at 5 GHz with 0″.4 resolution from the combined *A* and *B* configuration data. H is the hot spot. Contours are drawn at −1 (dotted), 2, 3, 4, 6, 8, 10, 12, 16, 20, 24, 30, 40, 50, 70, 100, 150, 200, 400, 600, 800, 1000 times 135 μJy per CLEAN beam area. The peak intensity is 194 mJy per CLEAN beam area.

are only rough guides to the total flux densities and angular sizes of the hot spots, since most of the hot spots are not well represented by Gaussian models. Among the results, we find:

• One clearly-identified hot spot for each lobe of 3C 20, 3C 22, 3C 55, 3C 244.1, and 3C 252.

• One hot spot, following our definition, in only one lobe for 3C 42, 3C 325, 3C 356, and 3C 441. 3C 325 has a jet "candidate": the hot spot is on the "possibly jetted" side. 3C 441 has a definite jet and the hot spot is also on the jetted side.

In the remaining sources, we have either insufficient resolution to apply our criterion in either lobe, or both hot spots are ill defined.

These results contrast with the Bridle *et al.* (1994a) sample, in which every QSR had at least one clear hot spot at this resolution. Thirteen of the QSR hot spots were on the jetted side, and eight on the counterjetted side, with the deficiency of counterjetted hot spots occurring among the larger sources in their sample. Bridle *et al.* (1994a) concluded that the extended 3CR quasars tend to lack counterjetted hot spots that meet the compactness criteria. For the 13 RGs, however, there is no apparent trend between hot spot occurrence and overall linear size of the source.

We have compared the largest linear size and the smallest linear size of the hot spot features (Table 7 of this paper and Table 12 of Bridle *et al.* 1994). A Kolmogorov–Smirnov test shows that the largest linear size distributions for the RGs and the QSRs are similar at the 17% significance level. For the smallest linear size, the two distributions are similar at the 1% significance level. The average value of the largest linear size is 2.1 and 2 kpc for the RGs and the QSRs, respectively. The average value of the smallest linear size is 1.43 and 1.24 kpc, respectively. The QSRs may have slightly more compact hot spots than RGs.

Bridle *et al.* (1994) also noted a trend among the quasars for the jetted hot spot to be the more compact *when there is a significant size asymmetry between it and the counterjetted hot spot*. They found that the ratio of the compactness of the jetted to that of the counterjetted hot spot depends on the apparent power of the compact central feature. We cannot duplicate these two investigations because of the

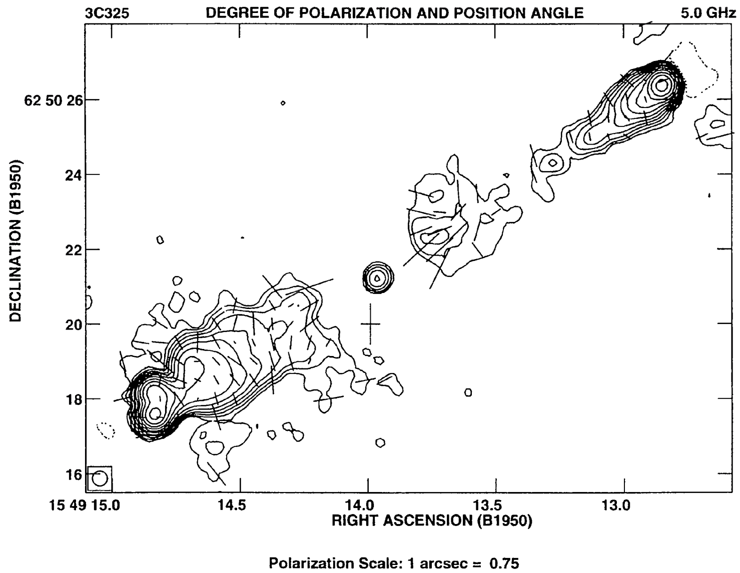

FIG. 17. Contour map of the total intensity of 3C 325 and its distribution of the degree of linear polarization and E-vector position angle at 5 GHz. Contours are drawn at −2 (dotted), 1, 2, 4, 6, 8, 16, 32, 64, 128, 256, 512, and 1024 times 120 μJy per CLEAN beam area. The peak intensity is 194 mJy per CLEAN beam area. A vector length of 1″ corresponds to $p=0.75$.

lack of jet and counterjet detections in the radio galaxies.

The mean logarithmic hot spot luminosities are 25.67 and 25.82 for the RGs and the QSRs, respectively. A K–S test shows that the distributions of hot spot luminosities are similar at the 50% significance level. Figure 28 plots the ratio of hot spot peaks (brightest to dimmest) within individual sources versus the compact central feature luminosity, for sources whose hot spots we can identify unambiguously. In terms of this ratio, there is no difference between the RGs and the QSRs.

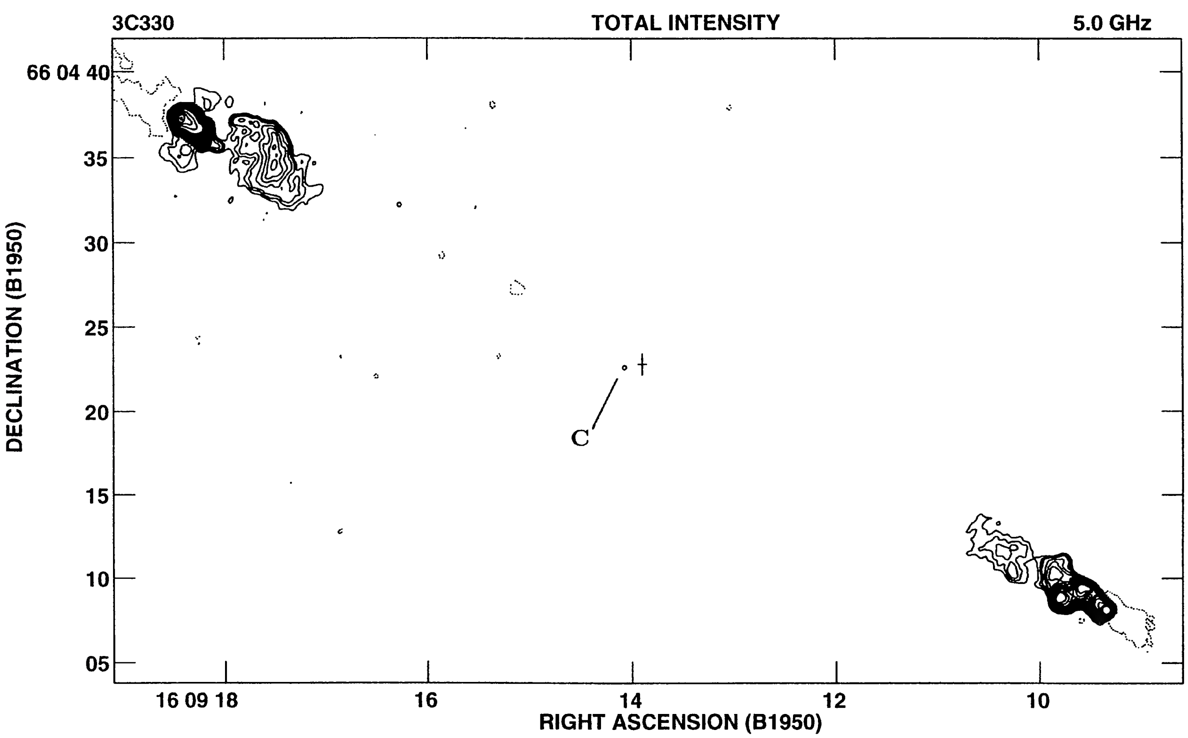

FIG. 18. Contour map of the total intensity of 3C 330 at 6 cm at 0.″43 resolution from the combined A and B configuration data. Contours are drawn at −1 (dotted), 2, 3, 4, 6, 8, 10, 12, 16, 20, 24, 30, 40, 50, 70, 100, 150, 200, 400, 600, 800, 1000 times 300 μJy per CLEAN beam area. The peak intensity is 308 mJy per CLEAN beam area.

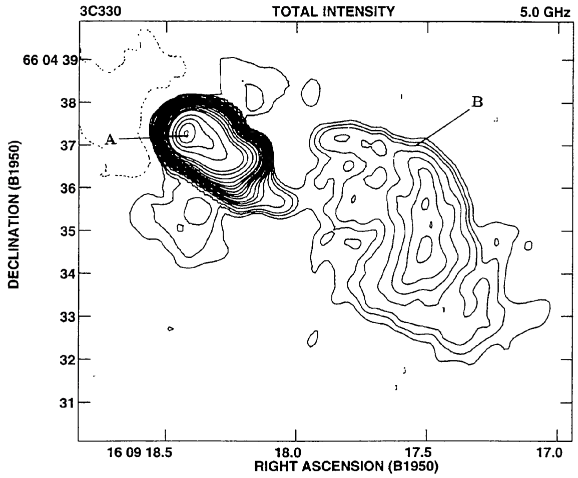

FIG. 19. Enlarged contour map of the total intensity of the NE lobe of 3C 330 at 5 GHz at 0."4 resolution.

4.4 Lobes

Table 8 lists the integrated flux densities of the lobes of the sample of RGs. As in Bridle *et al.* (1994)'s Table 15, these features do not include the flux densities of the embedded jet or counterjet candidates, if any. The AIPS task TVSTAT was used to measure the lobe flux densities. A background subtraction was also applied for these flux densities. Table 8 also shows the distances from the central features to the furthest point that can reliably be said to include lobe emission, as a measure of the ''largest extent'' of the lobe.

Figure 29 shows a histogram of the ratio of the flux density of the brightest lobe to the dimmest lobe for the two samples. The plot shows no difference between the RGs and the QSRs in terms of this ratio, with the exception of the high value of this ratio (about 14.5) for the quasar 3C 351. This explains the mean ratio of 4 for the QSRs, and 1.8 for the RGs. A K–S test was also run giving a 56% significance level of similarity between the two distributions. In another K–S test, we have compared the ratio of the logarithmic power of the brightest lobe to the dimmest lobe. The test shows that the two distributions are similar at the 60% significance level.

Figure 30 shows another histogram of the ratio of the hot spot luminosity to the lobe luminosity for the RGs and the QSRs. As reported above, there are 14 hot spots for the radio galaxies, and 21 hot spots for the quasars. The mean of this ratio for the RGs and the QSRs are 0.5 and 0.6, respectively. A K–S test shows that the distributions of this ratio for the two objects are similar at the 73% significance level.

Overall, the 13 RGs and the 13 QSRs show no difference in the prominence of their lobes. It is interesting to note here the striking similarity in the overall radio morphology between the RG 3C 244.1 and the QSR 3C 68.1.

5. DISCUSSION

The compact central radio features of 3C 42, 3C 244.1, 3C 252, 3C 325, and 3C 330 have been detected for the first time, and confirm the optical identifications. For 3C 441, there is a positional discrepancy of 1″ in δ between the optical nucleus and the compact central feature C. For 3C 325, we were unable to confirm the optical identification of Laing, and more accurate optical observations are desirable. Together with Paper I, we have detected 8 new radio compact central features out of the sample of 13 radio galaxies.

Definite radio jets were detected only in two RGs (3C 22 and 3C 441) and candidate jets or jet components in 3C 34, 3C 42, 3C 244.1, and 3C 325. Whether or not we exclude the jet of 3C 22, which shows hints of a broadline nuclear spectrum, these results are in strong contrast to the quasar

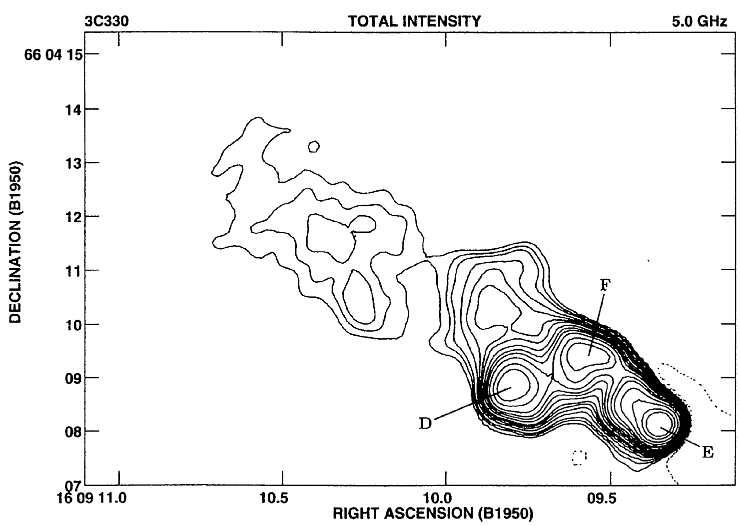

FIG. 20. Enlarged contour map of the total intensity of the SW lobe of 3C 330 at 5 GHz at 0."4 resolution.

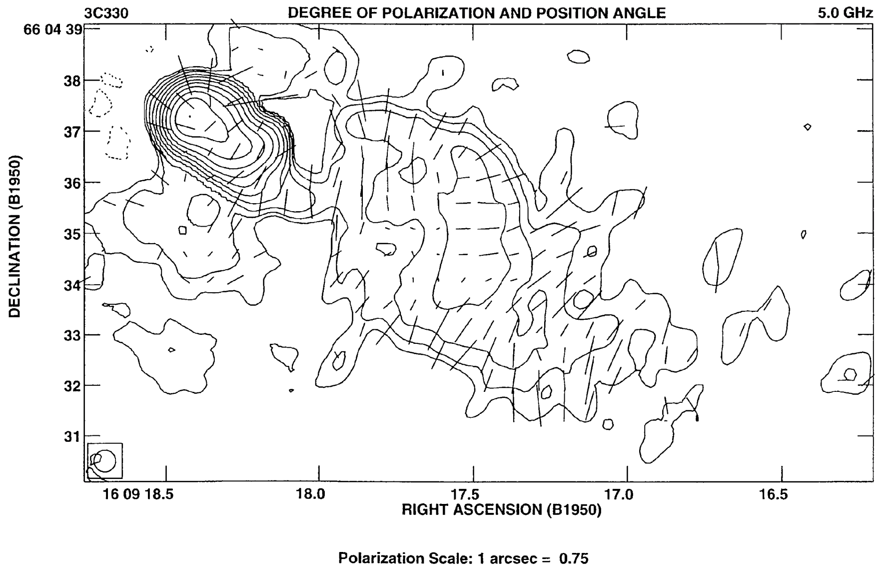

FIG. 21. Contour map of the total intensity of the NE lobe of 3C 330 and its distribution of the degree of linear polarization and E-vector position angle at 5 GHz. Contours are drawn at −2 (dotted), 1, 2, 4, 6, 8, 16, 32, 64, 128, 256, 512, and 1024 times 300 μJy per CLEAN beam area. The peak intensity is 308 mJy per CLEAN beam area. A vector length of 1″ corresponds to $p=0.75$.

sample, where Bridle *et al.* (1994) found 13 jets and six candidate counterjets in 13 objects.

This difference in jet detection rate is expected in the unification model if the quasar jets are closer to the line of sight, and thus more beamed towards the observer than galaxy jets. Figure 27 shows a plot of the jet/counterjet luminosity ratio versus the compact central feature for the 13 RGs and 13 QSRs.

In addition to the jet prominence, the QSRs are also distinguished by the prominence of their compact central features. The apparent luminosities of the compact central features for the RGs and the QSRs have very different distributions, with the QSRs showing more powerful radio central features. For the radio galaxies, the radio power of the central features ranges between $10^{22.9}$ and $10^{24.6}$ W Hz^{-1}, and for the quasars it ranges between 10^{24} and 10^{26} W Hz^{-1}. This difference in compact central feature power is much greater than the relatively small differences in total luminosity discussed in Sec. 2. Furthermore, the *ratio* of the compact central feature to extended flux densities $[S_{c.f}/(S_{\rm tot}-S_{c.f})]$ also differs significantly between the radio galaxies and quasars. The median of this ratio is 0.007 for the 13 RGs and 0.04 for the 13 QSRs. A K–S test shows that the two ratio distributions are similar at the 0.03% significance level. This

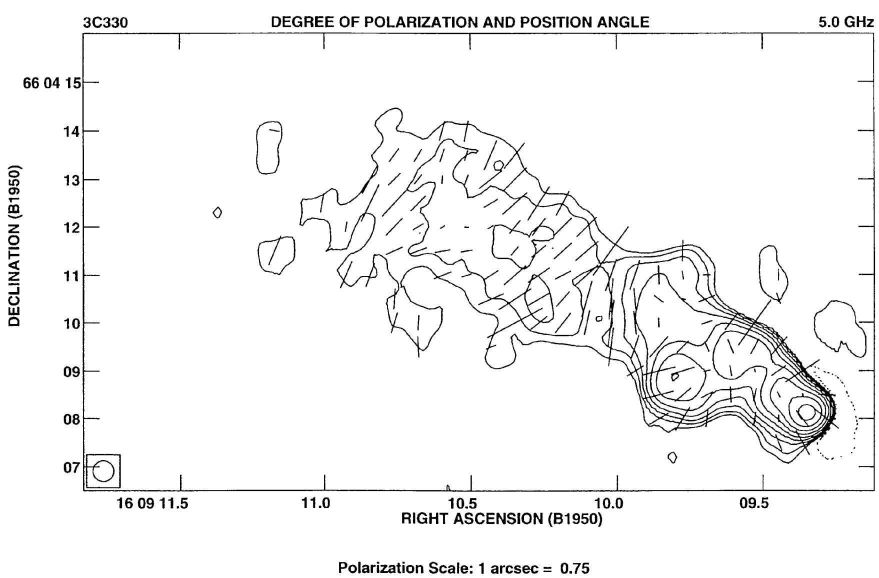

FIG. 22. Contour map of the total intensity of the SW lobe of 3C 330 and its distribution of the degree of linear polarization and E-vector position angle at 5 GHz superposed on contours from Fig. 21. A vector length of 1″ corresponds to $p=0.75$.

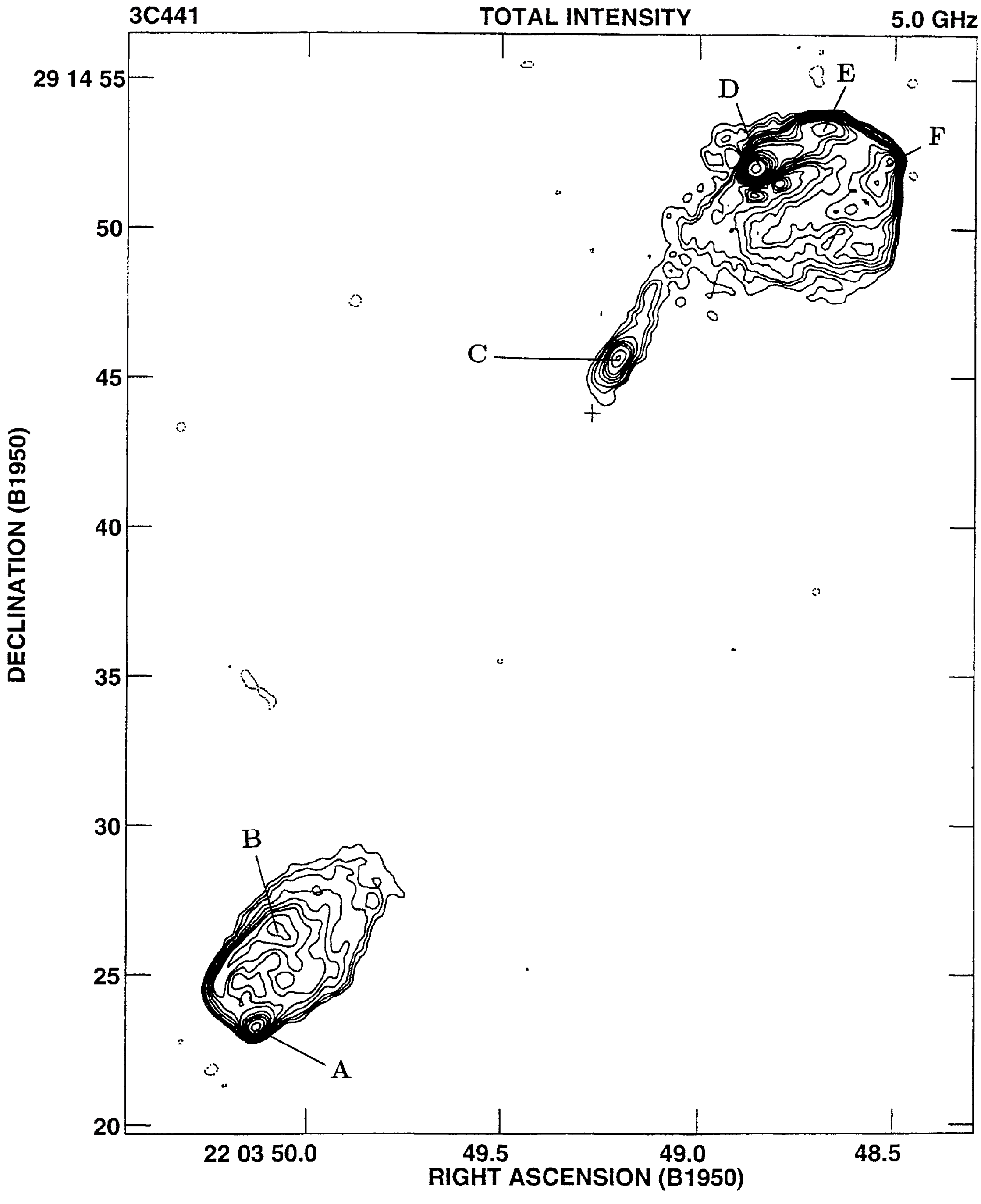

FIG. 23. 5 GHz contour map of the total intensity of 3C 441 at 0."38 resolution from the combined *A* and *B* configuration data. Feature D is the hot spot. Contours are drawn at −1 (dotted), 2, 3, 4, 6, 8, 10, 12, 16, 20, 24, 30, 40, 50, 70, 100, 150, 200, 400, 600, 800, 1000 times 140 μJy per CLEAN beam area. The peak intensity is 74 mJy per CLEAN beam area.

result is expected if the compact central features of the QSRs contain relativistically beamed jets; as pointed out by Orr & Browne (1982), the ratio could then indicate the orientation of a beamed radio source with respect to the line of sight.

In the relativistic beaming model, the jet/counterjet flux densities ratio is given by (Scheuer & Readhead 1979)

$$S_j/S_{cj}=\left(\frac{1+\beta_j\cos\theta}{1-\beta_j\cos\theta}\right)^{2+\alpha}, \tag{1}$$

where S_{cj} and S_j are the flux densities in the receding and the approaching jets, β_j is the velocity of the jet in units of c in the frame of the parent galaxy, θ is the angle with respect

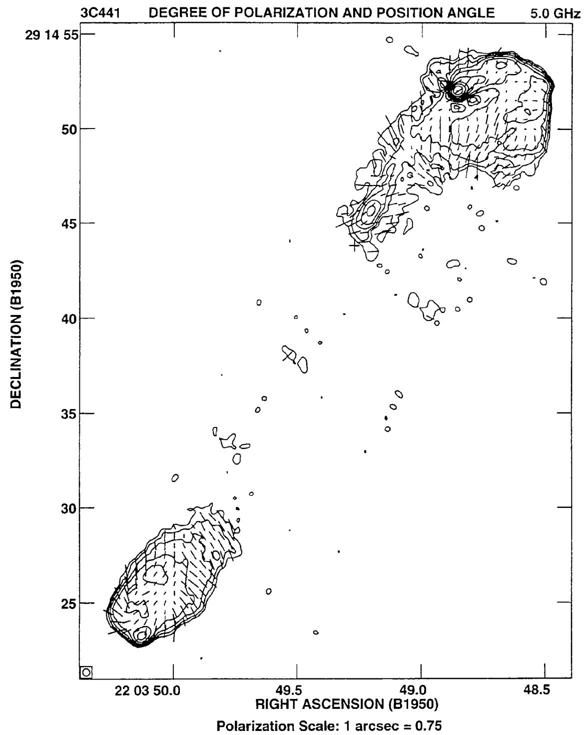

FIG. 24. Contour map of the total intensity of 3C 441 at 0."38 resolution and its distribution of the degree of linear polarization and E-vector position angle at 5 GHz. Contours are drawn at -2 (dotted), 1, 2, 4, 6, 8, 16, 32, 64, 128, 256, 512, and 1024 times 140 μJy per CLEAN beam area. The peak intensity is 74 mJy per CLEAN beam area. A vector length of 1″ corresponds to $p=0.75$.

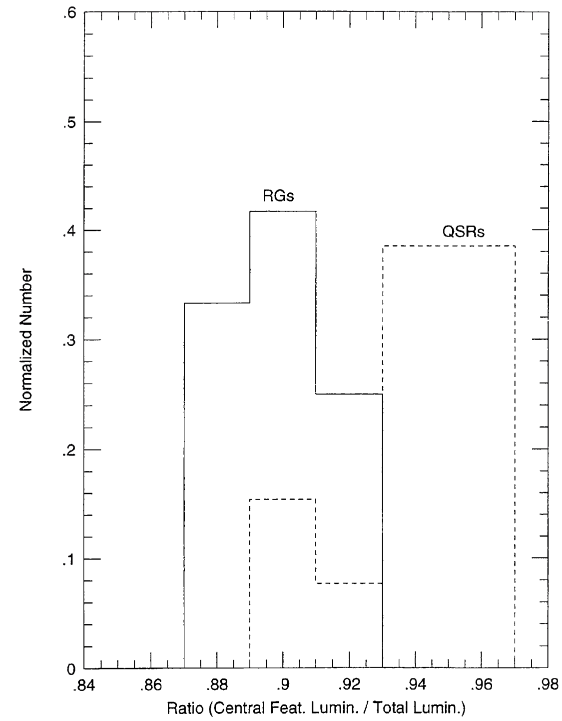

FIG. 26. Plot of the ratio of the compact central feature to the total luminosity for the two samples.

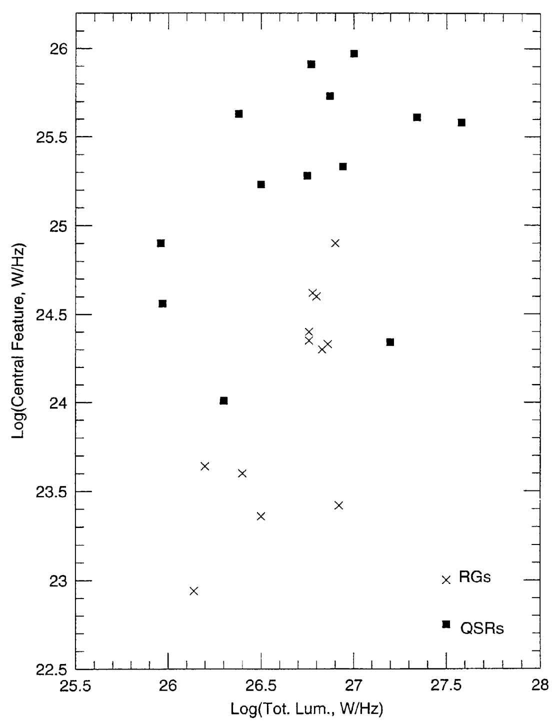

FIG. 25. Plot of the compact central feature luminosity of the source versus its total luminosity for the 13 QSRs and the 13 RGs.

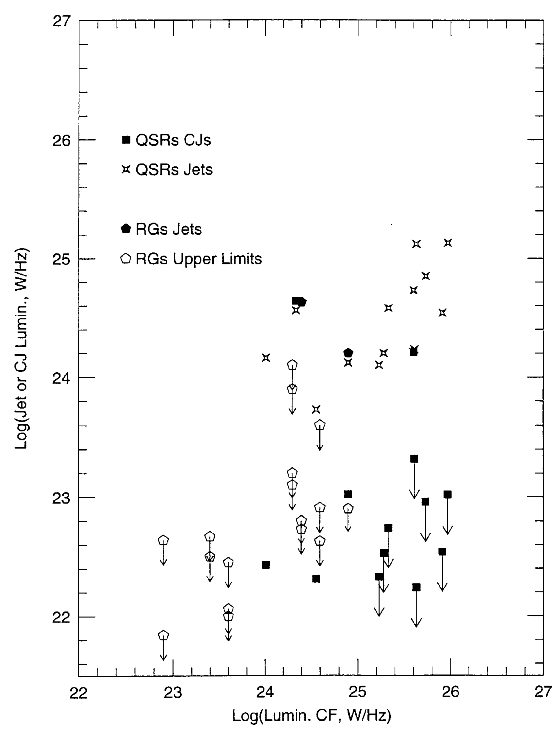

FIG. 27. Plot of the jet/counterjet luminosity versus the compact central feature for the RGs and QSRs discussed in Sec. *4.2*.

TABLE 7. Parameters of features reported in the images.

Source	Feature	Θ (″)	Peak $S_{5\ GHz}$ (mJy)	Integr. $S_{5\ GHz}$ (mJy)	LAS (″)	SAS (″)	p	χ
3C 20	A	26.6	35.7	101	1.2	0.4	0.3	22.6
	B*	23.3	125.1	147.3	0.5	0.4	0.1	-6.8
	D*	24.0	251.4	310.7	0.5	0.4	0.3	48.2
	E	25.2	93.6	394.5	1.8	0.4	0.2	-43.5
3C 22**	A*	10.4	141	234	0.6	0.4	0.05	-55.6
	B*	13.6	183.1	205	0.4	0.4	0.05	57
3C 34	A	24.0	4.8	18.1	1.5	0.4	0.3	76.1
	B	23.4	5.7	14.9	1.0	0.4	0.1	38.5
	C	14.9	1.05	2.1	0.8	0.4	0.1	-40.8
	D	12.6	0.6	1.6	1.0	0.4	< 0.05	—
	F	21.3	2.6	5.1	0.8	0.4	0.2	30.8
	G	23.4	1.9	5.8	1.2	0.4	0.26	-63.3
3C 42	A	14.9	40.3	106.1	1.1	0.4	0.05	37.1
	C*	13.9	62.1	126.2	0.8	0.4	0.2	-45.1
	D	14.2	57.9	77.7	0.6	0.4	0.2	44.1
3C 55	F1	20.5	1.0	2.5	0.9	0.4	0.2	-21.6
	F2	21.8	17.7	21.5	0.4	0.4	0.2	70.8
	F3	23.1	2.6	3.5	0.5	0.4	0.2	-53.9
	F4	25.6	1.4	4.2	1.0	0.4	0.5	52.0
	F5	26.5	1.5	2.4	0.6	0.4	< 0.05	—
	F6	28.0	14.5	18.5	0.5	0.4	0.3	-67.1
	F8*	29.7	37.5	76.7	0.7	0.4	0.1	28.5
	F9*	31	69	87	0.4	0.4	0.3	77.2
3C 244.1	A	24.7	41.6	64	0.6	0.4	0.2	-9.1
	B	23.2	39.7	82.3	0.9	0.4	0.3	64.2
	C*	18.7	10.8	12	0.5	0.4	0.4	-11.8
	E*	27.5	244	343	0.6	0.4	0.1	-22.6
3C 252	A	18.3	1.5	5.1	1.4	0.4	0.4	-49.7
	B	19.4	1.33	4.8	1.4	0.4	0.3	-34.7
	C*	19.7	8.3	11.2	0.5	0.4	0.3	-65.4
	E*	35.7	56.4	88.1	0.6	0.4	0.05	82.6
3C 265	A	47.8	6.9	22.2	1.3	0.4	0.2	98.2
	C	36.8	37.9	79.1	0.9	0.4	0.2	59.0
	E	31.3	90.6	162.4	0.7	0.4	0.1	-79.1
3C 324	A	—	56.1	69.8	0.4	0.3	0.1	-67
	C	—	0.5	0.7	0.5	0.3	< 0.02	—
	E	—	152.4	196.6	0.4	0.3	0.1	65.7
3C 325	A	7.0	198.2	239.7	0.5	0.4	0.2	84.5
	B	6.6	140.3	199.6	0.6	0.4	0.1	-1.8
	C	2.2	1.2	3.2	1.1	0.4	0.3	-61.5
	F	5.6	0.7	0.8	0.46	0.4	< 0.07	—
	H*	9.2	198.5	238.9	0.5	0.4	0.2	-77.7
3C 330	A	30.6	345.3	625.4	0.8	0.4	0.3	62.2
	D	29.6	23.9	59.9	1.1	0.4	0.4	-74.9
	E	32.5	112.2	148.7	0.6	0.4	0.3	41.5
3C 356	A	23.8	23.2	49.8	0.8	0.4	0.2	-48.4
	B	24.4	23.0	39.1	0.7	0.4	0.3	-18.3
	C	22.3	3.6	6.1	0.6	0.4	0.1	-77.7
	D	—	1.1	1.1	0.4	0.4	< 0.06	—
	E	4.7	0.5	0.5	0.4	0.4	< 0.06	—
	F*	48.4	30.3	57.6	0.7	0.4	0.2	-31.2
3C 441	A	25.4	7.0	15.1	0.8	0.4	0.2	-28.3
	C	—	3.5	10.1	1.1	0.4	< 0.03	—
	D*	7.9	82.5	103.3	0.5	0.4	0.3	-55.4

Notes to Table 7

Θ: angular distance between peak of feature and compact central feature
LAS, SAS: major and minor axes of fitted elliptical Gaussian component
p: fractional polarization (or 3σ upper limit) at position of peak
χ: apparent position angle of the $\vec{E}$ at the peak
*: Denotes a hot spot of the source
**: 3C 22 shows a quasar-like nucleus (Economou *et al.* 1995).

to the line of sight, and α is the spectral index of the jet ($S \propto \nu^{-\alpha}$). The corresponding Lorentz factor γ is then (Fernini 1991)

$$\gamma = \frac{1}{\{1-[1/(\cos^2\theta)][(s-1)/(s+1)]^2\}^{1/2}}, \tag{2}$$

where $s=(S_j/S_{cj})^{1/2+\alpha}$.

For the 13 QSRs, the jet side is always brighter than the counterjet side. By definition, this is also true for the RGs in

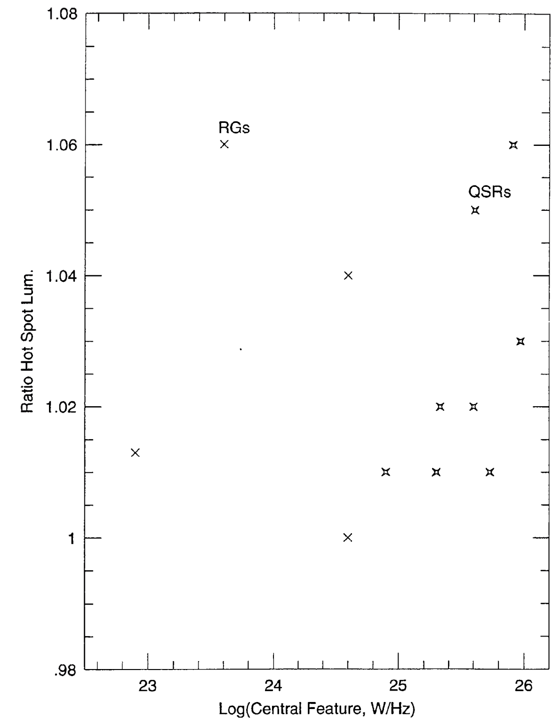

FIG. 28. Plot of the ratio of hot spot peak luminosity (brightest to dimmest) in terms of the compact central feature.

terms of the relativistic beaming model. This will allow us to perform a jet/counterjet analysis between the RGs and the QSRs sample. The jet/counterjet flux densities ratio for the 13 RGs will then be the ratio of the brighter to the dimmest side as reported in Table 6. Since most of these ratios (either

TABLE 8. Integrated properties of lobes.

Source	Side	Integrated Flux Density (mJy)	Log $L_{5\ GHz}$ (W/Hz)	Largest Extent (kpc)
3C 20	NW	1680	25.8	50.1
3C 20	SE	1280	25.7	53.3
3C 22*	NW	260	26.5	61
3C 22*	SE	361	26.7	47.4
3C 34	W	140	26.0	97.3
3C 34	E	180	26.1	101.3
3C 42	NW	372	25.9	47.7
3C 42	SE	465	26.0	51
3C 55	NW	247	26.3	123.2
3C 55	SE	295	26.4	128.4
3C 244.1	NW	543	26.1	94.4
3C 244.1	SE	421	26.0	84.5
3C 252	NW	180	26.5	89.8
3C 252	SE	92	26.2	159.4
3C 265	NW	286	26.4	133.3
3C 265	SE	387	26.6	201
3C 324	NE	430	27.0	—
3C 324	SW	165	26.6	—
3C 325	NW	309	26.5	41
3C 325	SE	650	26.8	31.7
3C 330	NE	1520	26.8	115.6
3C 330	SW	500	26.3	115
3C 356	NW	120	26.3	211
3C 356	SE	182	26.5	108.5
3C 441	NW	440	26.5	44
3C 441	SE	184	26.1	104

Note to Table 8

*: 3C 22 shows a quasar-like nucleus (Economou *et al.* 1995).

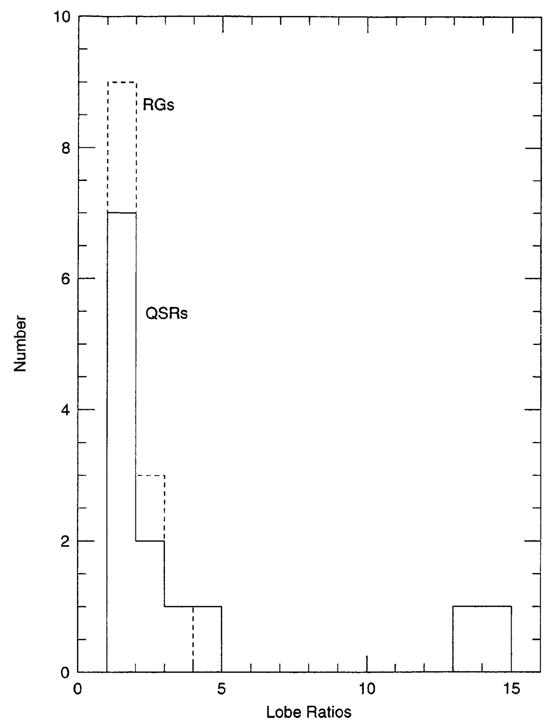

FIG. 29. Histogram of the ratio of lobe flux densities (brightest to dimmest) for the RGs and the QSRs.

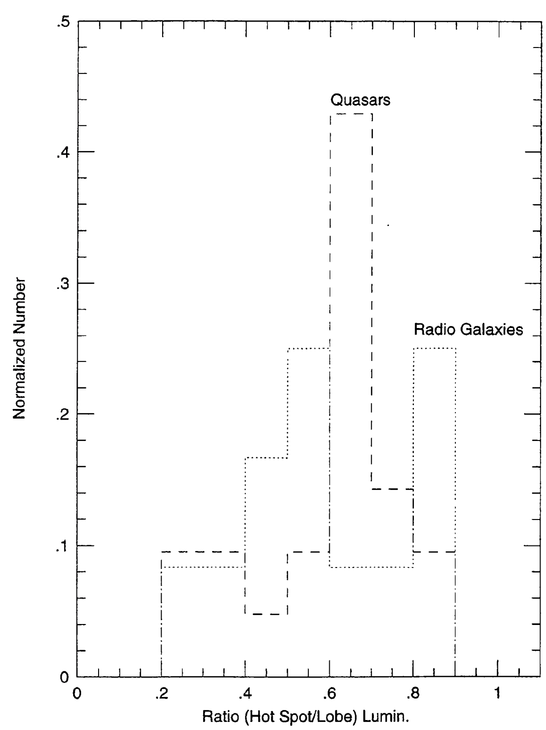

FIG. 30. Histogram of the hot spot luminosity to the lobe luminosity ratio for the 13 QSRs and the 13 RGs.

TABLE 9. Upper limits of the angle θ, Lorentz factor, and speed in units of c.

Source	S_j/S_{cj}	θ_{lim}	γ	β_{lim}
		13 RADIO GALAXIES		
3C 20	6.4	69	3.3	0.95
3C 22	20.2	58	5.4	0.98
3C 34	1.0	90	0.0	—
3C 42	1.0	90	0.0	—
3C 55	9.1	66	5.7	0.98
3C 244.1	2.8	78	2.9	0.94
3C 252	1.0	90	0.0	—
3C 265	1.0	90	0.0	—
3C 324	1.0	90	0.0	—
3C 325	4.7	73	6.2	0.99
3C 330	1.0	90	0.0	—
3C 356	10.0	65	5.5	0.98
3C 441	69	47	5.6	0.98
Median Val.	**2.8**	**78**	**2.9**	**0.94**
		13 QUASARS		
3C 9	3.3	76	2.7	0.93
3C 47	3.7	75	3.2	0.95
3C 68.1	1.2	88	5.3	0.98
3C 175	12	64	4.8	0.98
3C 204	27	55	4.7	0.98
3C 208	5.2	72	7.5	0.99
3C 215	26	56	8.5	0.99
3C 249.1	12	64	4.8	0.98
3C 263	34	53	5.1	0.98
3C 334	175	40	7.1	0.99
3C 336	9.5	65	3.7	0.96
3C 351	52	50	12.3	0.99
3C 432	4.7	73	6.2	0.99
Median Val.	**12**	**64**	**4.8**	**0.98**

Note: The bold face numbers correspond to the median values of the two samples

for the QSRs or the RGs) are lower limits, we will just take their face values for this simple comparative study. If we require the term under the square root in Eq. (2) to be positive, a limit on the angle θ can be set for each RG and QSR. Table 9 gives the upper limits for $\theta_{\rm lim}$, the corresponding Lorentz factors, and the jet speed in units of c. As required by the model, Table 9 shows that sources with high jet/counterjet ratio have lower values of $\theta_{\rm lim}$ than sources with low ratios. In other words, sources with high ratios are less oriented with respect to the line of sight than sources with low ratios. This conclusion seems to be true for both RGs and QSRs. Therefore, there is no clear difference between the two sample in terms of $\theta_{\rm lim}$. We should stress the point here that the value of $\theta_{\rm lim}$ are upper limits, and thus the values listed in Table 9 could then be lower. This caveat should be kept in mind when interpreting $\theta_{\rm lim}$ for the QSRs and the RGs. The median value of the jet/counterjet ratio for the QSRs is 12, corresponding to a $\theta_{\rm median}\leq 64°$. The median value of this ratio for the RGs is 2.8, corresponding to $\theta_{\rm median}\leq 78°$. The value of $\theta_{\rm median}$ for the RGs is thus larger than the value of $\theta_{\rm median}$ for the QSRs, meaning that the RGs are more oriented toward the plane of the sky than the QSRs.

In terms of Lorentz factors, the median values are 2.9 and 4.8 for the RGs and QSRs, respectively. At these values, the jets of both QSRs ($\approx 0.98c$) and RGs ($\approx 0.94c$)are highly relativistic.

In is interesting to note that the $\theta_{\rm lim}$ of 58° for 3C 22 and $\theta_{\rm lim}$ of 47° for 3C 441 (the only two RGs with definite jet detection) are below the $\theta_{\rm median}$ of 64° for the 13 QSRs. We pointed out earlier that 3C 22 shows a quasar-like nucleus (Economou *et al.* 1995). In Sec. *3.8*, we noted the uncertainty in the optical identification of 3C 441. The numbers (S_j/S_{cj}, θ, or γ) related to these two sources are not different from those of the 13 QSRs (Table 9).

In Sec. *4.3* we reported some statistics regarding the hot spot compactness. A K–S test shows that for the smallest linear size, the two distributions are similar at the 2% significance level, while for the largest linear size the two distributions are similar at the 28% level. We may see here a difference in compactness between the QSRs and the RGs, with the QSRs showing more compact hot spots. How do we account for differences in compactness between the hot spots of the RGs and the QSR? Two possible scenarios may account for such differences. First, some of the hot spot emission is beamed, i.e., that bulk relativistic motion persists as far as, even through, the hot spots as suggested by Laing (1989). Laing further pointed out that nonaxisymmetric flow model (in which the shocks are oblique) is crucially different because it allows the post-shock to remain supersonic, and (given high obliquity) possibly relativistic so that beaming can remain significant. Komissarov (1993) and Komissarov & Falle (1996) have performed relativistic flow simulations that reinforced the idea that relativistic flow can survive up to the hot spot. These simulations have shown that the Doppler boosting of radio emission from the high pressure part of the backflow creates a leading arc in the hot spot whose speed can be close to $c/\sqrt{3}$ in the case of relativistic jet. This is large enough to cause significant beaming at the hot spot (Komissarov & Falle 1996).

Second, the relativistic beaming alone may be inadequate. However, if we couple the time delay effects with hydrodynamical effects, such differences in hot spots compactness might be attributed to evolutionary processes. Norman *et al.* (1984) and Burns *et al.* (1991) have noted that numerical simulations of radio jets clearly demonstrate that the "working surface" at the head of the jet is very dynamic. The size and position of the Mach disk (i.e., hot spot) vary dramatically with time. At certain epochs, the Mach disk even disappears, only to reappear a short time later. For the QSRs and the RGs, the difference in viewing time for the hot spots might allow us to see two slightly different epochs in the evolution of the jet's working surfaces.

Overall, we conclude that the unification scheme of Barthel (1989) can account for major differences between the RG and QSR sample in jet detection and compact central features prominence, but perhaps not for hot spot compactness. As noted by Bridle *et al.* (1994), the flip-flop model should be dealt with as a two-beam model with a variable, but finite, power asymmetry in order to account with the presence of bright compact hot spots on the sides with no counterjet candidates.

Other effects that may influence the symmetries of the radio structure include large-scale gradients in the environments of the quasars and the radio galaxies (tested with [O II] image in Paper I). It will be interesting to extend such tests to the quasar sample.

Most of the data calibration and image processing was done at New Mexico State University. I.F. is indebted to NMSU for its hospitality during an extended visit to analyze these data. We are very thankful for the comments of A.H. Bridle regarding the overall organization of this paper. This work was supported in part by NSF Grant No. AST-9317596 to J.O.B. We are indebted to the NRAO AIPS group for their software for VLA data reduction and image processing.

REFERENCES

Alexander, P., & Leahy, J. P. 1987, MNRAS, 225, 1
Barthel, P. D. 1989, ApJ, 336, 606
Blandford, R. D., & Königl, A. 1979, ApJ, 232, 34
Bridle, A. H., & Perley, R. A. 1984, ARA&A, 22, 319
Bridle, A. H., Hough, D. H., Lonsdale, C. J., Burns, J. O., & Laing, R. A. 1994, AJ, 108, 766
Burns, J. O., Norman, M. L., & Clarke, D. A. 1991, Science, 253, 522
Economou, F., Lawrence, A., Ward, M. J., & Blanco, P. R. 1995, MNRAS, 272, L5
Fanaroff, B. L., & Riley, J. M. 1974, MNRAS, 167, 31P
Fernini, I., Burns, J. O., Bridle, A. H., & Perley, R. A. 1993, AJ, 105, 1690 (Paper I)
Fernini, I. 1991, Ph.D. thesis, University of New Mexico
Fomalont, E. B., & Perley, R. A. 1989, in NRAO Workshop No. 21: Synthesis Imaging in Radio Astronomy, ASP Conf. Ser. 6, edited by R. A. Perley, F. R. Schwab, and A. H. Bridle (ASP, San Francisco), p. 113
Garrington, S. T., Conway, R. G., & Leahy, J. P. 1991, MNRAS, 250, 271
Hiltner, P. R., Meisenheimer, K., Röser, H.-J., Laing, R. A., & Perley, R. A. 1994, A&A, 286, 25
Johnson, R. A., Leahy, J. P., & Garrington, S. T. 1995, MNRAS, 273, 877
Komissarov, S. S. 1993, in Jets in Extragalactic Radio Sources, edited by H.-J. Röser and K. Meisenheimer (Springer, Berlin), p. 45
Komissarov, S. S., & Falle, A. E. G. 1996, in Energy Transport in Radio Galaxies, ASP Conf. Ser. 100, edited by P. E. Hardle, A. H. Bridle, and J. A. Zensus (ASP, San Francisco) p. 327
Laing, R. A. 1982, in Extragalactic Radio Sources, IAU Symposium No. 97, edited by D. S. Heeschen and C. M. Wade (Reidel, Dordrecht), p. 161
Laing, R. A. 1988, Nature, 331, 149
Laing, R. A. 1989, in Hot Spots in Extragalactic Radio Sources, edited by K. Meisenheimer and H.-J. Röser (Springer, Berlin), p. 27
Laing, R. A., Longair, M. S., Riley, J. M., Kibblewhite, E. J., & Gunn, J. E. 1978, MNRAS, 183, 547
Laing, R. A. Riley, J. M., & Longair, M. S. 1983, MNRAS, 204, 151
Lawrence, C. R., Pearson, T. J., Readhead, A. C. S., & Unwin, S. C. 1986, AJ, 91, 494
Leahy, J. P., & Perley, R. A., 1991, AJ, 102, 537
Leahy, J. P., & Williams, A. T. 1984, MNRAS, 210, 929
Miley, G. K., 1980, ARA&A, 18, 165
Norman, M. L., Winkler, K.-H. A., & Smarr, L. 1984, in Proceedings of NRAO Workshop 9: Physics of Energy Transport in Extragalactic Radio Sources, edited by A. H. Bridle and J. A. Eilek (NRAO, Green Bank), p. 150
Orr, M. J. L., & Browne, I. W. A. 1982, MNRAS, 100, 1067
Rees, M. J. 1978, MNRAS, 184, 61P
Scheuer, P. A. G., & Readhead, A. C. S. 1979, Nature, 277, 182
Spinrad, H., Djorgovski, S., Marr, J., & Aguilar, L. 1985, PASP, 97, 932